

1 **Novel engineered high performance sugar beetroot 2D nanoplatelet-cementitious**  
2 **composites**

3  
4 Hasan Hasan<sup>1</sup>, Bo Huang<sup>1</sup>, Mohamed Saafi<sup>1\*</sup>, Jiawei Sun<sup>2</sup>, Yin Chi<sup>1</sup>, Eric Whale<sup>3</sup>, David  
5 Hepworth<sup>3</sup>, Jianqiao Ye<sup>1</sup>

6 <sup>1</sup>Department of Engineering, Lancaster University, Lancaster, LA1 4YW, UK

7 <sup>2</sup>Shaanxi Key Laboratory of Safety and Durability of Concrete Structures, Xijing University,  
8 Xi'an, China

9 <sup>3</sup>Cellucomp Ltd, Burntisland, Fife, KY3 9DW, UK

10

11

12 \*Corresponding author. Tel. 44 (0) 1524 594070

13 Email: m.saafi@lancaster.ac.uk (M.Saafi)

14

15 **Abstract**

16 In this paper, we show for the first time that environmentally friendly nanoplatelets synthesized  
17 from sugar beetroot waste with surface area and hydroxyl functional groups similar to those of  
18 graphene oxide (GO) can be used to significantly enhance the performance of cementitious  
19 composites. A comprehensive experimental and numerical simulation study was carried out to  
20 examine the performance of the bio waste-derived 2D nanoplatelets (BNP) in cementitious  
21 composites. The experimental results revealed that the addition of BNPs decreased the workability  
22 of the cement pastes due to their high surface area and dominant hydrophilic functional groups.  
23 The experimental results also revealed that the BNP sheets altered the morphology of the hydration  
24 phases of the cementitious composites. At 0.20-wt%, the BNP sheets increased the content of the  
25 C-S-H gels. At higher concentrations (i.e., 0.40-wt% and 0.60-wt%), however, the BNP sheets  
26 increased the content of the calcium hydroxide (Ca(OH)<sub>2</sub>) products and altered their sizes and  
27 morphologies.

28 The flexural results demonstrated that the 0.20-wt% BNPs produced the highest flexural strength  
29 and modulus elasticity and they were increased by 75% and 200%, respectively. The numerical  
30 simulations were in good agreement with the fracture test results. Both results showed that the  
31 0.20-wt% BNPs optimal concentration significantly enhanced the fracture properties of the

32 cementitious composite and produced mixed mode crack propagation as a failure mode compared  
33 to Mode I crack propagation for the plain cementitious composite due to combined crack bridging  
34 and crack deflection toughening mechanisms. Because of this, the fracture energy and the fracture  
35 toughness were increased by about 88% and 106%, respectively.

## 36 **1. Introduction**

37 A great deal of research efforts has been devoted to improving the performance of cementitious  
38 composites using different nanoscale additives. Such additives offer tremendous promise for a  
39 wide range of uses in cementitious materials that could result in sustainable and high performance  
40 concrete structures with intelligence and multifunctional capabilities [1, 2]. For example,  
41 cementitious composites incorporating reactive nanoparticles such as nano-SiO<sub>2</sub> [3,4], nano-TiO<sub>2</sub>  
42 [5, 6] and nano-CaCO<sub>3</sub> [7, 8] were found to exhibit improved mechanical properties and durability  
43 characteristics. This is because the high specific area of nanoparticles accelerates the hydration of  
44 cement, resulting in more Calcium Silicate Hydrate (C-S-H) gels. Furthermore, due to their small  
45 particle size, the nanoparticles tend to act as fillers, which results in a denser microstructure.  
46 However, these reactive nanoparticles tend to agglomerate at high concentrations and, due to their  
47 low aspect ratios, they cannot arrest the propagation of cracks, thereby are unable to enhance the  
48 fracture properties of cementitious composites [9].

49 A significant body of research has demonstrated the benefits of adding carbonaceous nano-  
50 additives such as carbon nanotubes (CNTs), carbon nanofibers (NFs) and graphene oxide (GO) to  
51 cementitious materials. However, CNTs and NFs were shown to provide limited improvements  
52 in the mechanical properties due to their agglomeration and lack of chemical and mechanical  
53 bonding with the cement composite matrix [10, 11]. The two dimensional (2D) GO is being  
54 considered as an ideal candidate for reinforcing cementitious composites due to its distinctive

55 properties such as large specific area, excellent mechanical properties and high dispersibility in  
56 water due to hydroxyl functional groups on its surface [12]. Studies reported that GO accelerates  
57 the hydration of cement and, regulate the growth and morphology of the hydration phases, leading  
58 to improvement in the mechanical properties of GO composites [13-15]. Studies also reported that  
59 GO influences pore volume distribution in cementitious materials [16]. It was shown that GO  
60 reduces the capillary pores and fills the micropores in the cement matrix [17]. Because of its large  
61 specific area, GO was found to bridge microcracks, thereby enhancing the stiffness and the fracture  
62 resistance of the cement matrix [18]. However, large-scale production of nano-SiO<sub>2</sub> nano-TiO<sub>2</sub>,  
63 nano-CaCO<sub>3</sub>, CNTs, NFs and GO and their applications in cementitious materials have been  
64 hampered by the high costs, un-scalability, complex manufacturing processes and, environmental,  
65 health and safety risk issues.

66 In this paper, we investigate for the first time the performance of cementitious composites  
67 containing novel and environmentally friendly low-cost 2D BNP sheets. The BNP sheets were  
68 produced from renewable materials such as sugar beetroot waste and resemble GO in terms of  
69 large specific area, excellent mechanical properties and hydroxyl functional groups with excellent  
70 dispersibility in water. The effect of different BNP concentrations on the workability, hydration  
71 phases, microstructure and mechanical properties was examined. The cracking behavior and the  
72 failure mode of the BNP cementitious composites were also examined and validated using  
73 numerical modelling.

## 74 **2. Experimental Program**

### 75 *2.1 Preparation of BNPs*

76 The BNP sheets were produced and supplied by our industrial partner Cellucomp Ltd, UK. The  
77 BNP sheets were synthesized from sugar beetroot waste recovered from existing industrial

78 processes. The isolation of BNPs from sugar beetroot pulp is detailed in [19]. In summary, this  
79 process involves alkali treatment of recovered sugar beetroot pulp with 0.5M of potassium  
80 hydroxide (KOH) to extract the hemicellulose and pectin from the cells. The resulting mixture  
81 was heated to 90°C for 5 hours and homogenized for 1 hour with a rotating mixer at rates between  
82 11 and 30 m/s. This homogenization process separates the cells along the line of the middle lamella  
83 and breaks the separated cells into BNP sheets with about. The mixture was then filtered to remove  
84 the dissolved materials. Finally, a nonionic surfactant (Span<sup>TM</sup> from Croda PLC, UK) was added  
85 to the BNP paste to coat the surface of the platelets to reduce aggregation thereby allowing BNPs  
86 to be readily dispersed in aqueous solutions [19].

## 87 *2.2. Preparation of BNP cement pastes*

88 Portland cement (OPC) type CEM I 52.5N was used to prepare the cementitious composites with  
89 a water-to-cement ratio of 0.35. Commercially available superplasticizer (Glenium 51) was used  
90 at a concentration of 1-wt% to enhance the workability of the cement pastes. The cement pastes  
91 were modified with BNPs at concentrations of 0.20, 0.40 and 0.60-wt%. The BNP was used as-  
92 received and consisted of a paste with 4% solid and 96% water. The as-received BNPs were first  
93 added to the required water and superplasticizer, followed by mild sonication for 30 min using a  
94 probe sonicator. The resulting suspension was then blended with the cement and mixed for 7 min.  
95 For each BNP loading, 24 prisms (40 mm× 40 mm× 160 mm) were prepared to determine the  
96 mechanical and fracture properties of the cementitious composites. The prisms were demolded  
97 after 24 hrs then left to cure in water at a temperature of 21 °C for 7, 14 and 28 days.

## 98 *2.3. Characterization of BNPs*

99 Optical microscopy and ultraviolet-visible spectrophotometer were employed to examine the  
100 dispersion properties and stability of BNPs at sonication times of 30, 50 and 100 min. Scanning

101 electron microscopy (SEM) (JSM-7800F) fitted with X-ray Energy Dispersive Spectrometer  
102 (EDS) and X-ray diffraction (XRD) were used to determine the chemical composition,  
103 morphology and microstructure of the BNP sheets. The EDS consisted of a X-max50 silicon drift  
104 detector with an area of 50 mm<sup>2</sup>. The elemental analysis was conducted at a voltage of 10 kV  
105 under ambient temperature. The XRD system consisted of Rigaku SmartLab equipped with a Cu  
106 rotating anode operating at 45kV and 200mA, a Ge(220) double bounce monochromator and a  
107 Dtex-250 1d detector. The samples were analyzed with  $\theta/2\theta$  scans with a rate 3 deg./min, under  
108 ambient conditions. An Agilent Technologies Exoscan 4100 Fourier transform mid-infrared  
109 spectrometer (FTIR) with diffuse sample interface was used to collect infrared diffuse spectra in  
110 the range of 500–5000 cm<sup>-1</sup>. The instrumental conditions for spectral collection were 128 scans at  
111 a resolution of 8 cm<sup>-1</sup> under ambient conditions. The spectral changes both in terms of size and  
112 position were used to identify the processes and chemical changes in the BNP sheets.  
113 Thermogravimetric analysis (TGA) was carried to study the thermal stability of BNPs under  
114 temperatures between 25 and 1100°C at a rate of 10 °C/min in nitrogen (N<sub>2</sub>).

#### 115 *2.4. Measurement of workability*

116 The effect of the BNP sheets on the workability of the cement pastes was assessed using a mini-  
117 slump cone with a top diameter of 70 mm, a bottom diameter of 100 mm and a height of 60 mm.  
118 For each BNP concentration, the mini-slump diameter was measured according to [20]. The  
119 average mini-slump diameter was based on three measurements.

#### 120 *2.5. Characterization of hydration and microstructure BNP cementitious composites*

121 Samples were collected from the fractured flexural prisms at 7, 14 and 28 days to examine the  
122 effect of BNP concentration on the hydration and microstructure of the cementitious composites.  
123 TGA measurements were performed to estimate the degree of hydration (DOH) and the content of

124 Ca(OH)<sub>2</sub>. In this experiment, the samples were heated from 25 to 1100 °C at a rate of 10 °C/min  
125 under nitrogen (N<sub>2</sub>). In addition, TGA measurements were performed on BNPs and cement  
126 particles for correction purposes [21]. XRD analysis was carried out to further investigate the  
127 DOH and determine the crystallinity of the hydration phases. SEM was employed to determine  
128 the microstructure characteristics of the BNP-cementitious such as distribution of BNPs and crack  
129 bridging mechanism. Transition electron microscopy (TEM) analysis was also conducted to study  
130 the microstructure alteration processes associated with the addition of BNPs.

### 131 *2.6. Mechanical and fracture characterization of BNP cement composites*

132 As shown in Figs. 1a and 2a, four-point bending tests were conducted on 48 cementitious  
133 composite prisms (40 mm × 40 mm × 160 mm) (12 prisms per BNP concentration) under  
134 displacement control with a rate of 0.1 mm/min. The flexural strength and modulus of elasticity  
135 of the prisms were determined. Additionally, 48 cementitious prisms (40 mm × 40 mm × 160 mm)  
136 equipped with a notch (3 mm x 16 mm) at the mid-span were subjected to a three-point bending  
137 test to evaluate the effect of BNPs on the fracture resistance of the prisms (Fig. 1b). The three-  
138 point bending tests were also carried out under displacement control with a rate of 0.03 mm/min.  
139 The crack mouth opening displacement (CMOD) was measured with a video gauge<sup>TM</sup> acquired  
140 from Imetrum LTd. The video gauge system consisted of two lenses, an iMetrum controller and  
141 a data acquisition system. As can be seen in Fig. 2b, five lines of 6 black dots with a dot diameter  
142 of 4 mm and a center-to-center spacing of 5 mm were printed on the surface of the prisms around  
143 the notch to define the region where the displacement is measured. The lenses were placed 1.5 m  
144 away from the surface of the prisms (Fig. 2c). During testing, the positions of the dots were  
145 continuously monitored by the lenses (Fig. 2c), and recorded along with the load. Both load and  
146 positions were recorded at a frequency of 15 Hz. The CMOD was obtained by monitoring the

147 horizontal displacement between the two dots adjacent to the mouth of the crack as shown in Fig.  
148 1b. The load vs CMOD, and the calculated fracture energy and fracture toughness were employed  
149 to quantify the contribution of BNP to the fracture resistance of the cementitious composites.

### 150 **3. Results and discussion**

#### 151 *3.1. Characterization of BNP sheets*

152 The chemical components of the BNP sheets obtained from the EDX elemental analysis are given  
153 in Table 1. As indicated in this table, the BNPs sheets contain mostly carbon, oxygen and  
154 hydrogen. The main chemical components are carbon 47.61% and oxygen 46.91%. The BNP  
155 sheets contain some sodium and chloride impurities as a result of their chemical treatments. The  
156 XRD pattern of the BNP sheets is shown in Fig. 3. As can be seen, the sheets exhibit two main  
157 peaks at  $2\theta = 15$  and  $22$ , which represents the structure of cellulose. The XRD pattern suggests  
158 that the structure of the BNP sheets can be divided into two regions. The narrow peak at  $2\theta = 15$   
159 represents the crystalline region of BNPs with a surface (110) plane. This surface (110) plane is  
160 hydrophilic in nature due to the exposure to a large number of hydroxyl (OH) groups, thus, has a  
161 good dispersion in water [22]. The somewhat broad peak at  $2\theta = 22.5$  with surface (200) plane  
162 indicates the presence of crystalline and amorphous regions of BNPs. The amorphous region is  
163 associated with the amorphous lignin and hemicellulose components of BNPs. The crystalline  
164 region is highly hydrophobic because of the existence of C-H moieties [22]. The crystallinity  
165 index (CI) of BNPs was calculated using the following equation [22]:

$$166 \quad CI (\%) = 100 \times \frac{I_{002} - I_{am}}{I_{002}} \quad (1)$$

167 where  $I_{002}$  is the intensity of the XRD peak at  $2\theta = 22.5$  and plane (200);  $I_{am}$  is the intensity of the  
168 amorphous cellulose between the planes (200) and (110) at  $2\theta = 18$ . The calculated average  $CI$

169 was about 64% which indicates high tensile strength and stiffness of the BNP sheets [22]. As a  
170 result, the proposed BNP sheets are good candidate materials for reinforcing cementitious  
171 composites. The FTIR spectrum of BNPs shown in Fig. 4 is similar to that reported by Li et al.  
172 [21]. This figure shows that the absorption in the  $3600\text{ cm}^{-1}$ - $3000\text{ cm}^{-1}$  region is the result of the  
173 vibrational stretching bands of hydrogen bonded hydroxyl groups which indicates the hydrophilic  
174 nature of the BNP sheets [22]. The pronounced peak at  $2900\text{ cm}^{-1}$  is attributed to the stretching  
175 vibration of saturated C-H in cellulose [22] and the peak at  $1030\text{ cm}^{-1}$  is associated with the  
176 bending vibration of the absorbed water molecules [22]. Figure 4 shows that asymmetric and  
177 symmetric bending vibration bands exist at  $1371\text{ cm}^{-1}$  and  $1443\text{ cm}^{-1}$  [22].

178 The TGA/DTA results shown in Fig. 5 illustrate the thermal stability of BNPs. As depicted, the  
179 BNP sheets exhibit a small mass loss when heated from 25 to  $200^{\circ}\text{C}$  due to the evaporation of  
180 water content. A significant mass loss is observed between 200 and  $700^{\circ}\text{C}$  as a consequence of  
181 elimination of hydroxyl groups and decomposition of the carbon chains [21]. The mass loss  
182 remains constant at temperatures between 700 and  $1100^{\circ}\text{C}$ . The DTA spectrum shows a sharp  
183 peak at a temperature of about  $260^{\circ}\text{C}$  due to the dehydration of BNP sheets and a broad peak at  
184 about  $500^{\circ}\text{C}$  due to the decomposition of the BNP sheets. Overall, the BNP sheets exhibit a good  
185 thermal stability in the temperature range of 25 to  $100^{\circ}\text{C}$ , which is the range in which cementitious  
186 composites are typically operating.

187 Figure 6 shows a typical micrograph of the BNP sheets, which indicates that the BNP sheets have  
188 a wrinkled texture resulting from the treatment of the sugar beetroot. This texture typically consists  
189 of crumpled and, stacked and overlapped thin sheets. This morphology enables the BNP sheets to  
190 interact mechanically with cement matrix, thus significantly enhancing the overall mechanical  
191 properties of the BNP composites [17]. It can be seen from Fig. 6 that the BNP sheets are

192 composed of randomly oriented stacked nanofibers with a diameter of about 10 nm. It worth  
193 mentioning that it was not possible to measure the dimensions of the BNP sheets, however,  
194 according to the supplier, the average diameter of the flakes is about 50  $\mu\text{m}$ .

### 195 *3.2. Colloidal properties and stability of BNP aqueous solutions*

196 The colloidal properties and stability of the BNP aqueous suspensions were determined in terms  
197 of state of aggregation and microscale dispersion in aqueous solutions. Figure 7b depicts a typical  
198 optical microscope image of the prepared BNP aqueous suspensions shown in Fig. 7a. As can be  
199 seen, the BNP sheets seem to be uniformly dispersed without agglomeration. Figure 8 shows the  
200 UV-vis spectroscopy spectra of the BNP aqueous solution as a function of sonication time. As  
201 shown, the absorbance of the BNP sheets exhibits a maximum between 300 and 320 nm at all  
202 sonication times. As the sonication time increases, the area under the spectrum lines representing  
203 the absorbance increases as well, resulting in highly dispersed BNP sheets in water. It is worth  
204 noting that the optical microscope image and absorbance spectra remained unchanged after 1 year,  
205 thus indicating good stability of the BNP aqueous solutions.

### 206 *3.3. Influence of BNP on the workability of cement pastes*

207 Figure 9 shows the effect of the BNP sheets on the workability of the cement pastes. As can be  
208 seen, the addition of 0.20-wt% BNPs did not affect the slab diameter of the cement paste, however,  
209 the addition of 0.40-wt% BNPs and 0.60-wt% BNPs leads to a reduction in the slab diameter of  
210 approximately 80% and 90%, respectively, compared to the control mix. The slump decreases as  
211 the content of BNPs increases, which indicates that the slump loss is proportional to the content of  
212 BNPs. This is attributed to the high hydrophilicity and large specific area of the BNP sheets,  
213 thereby requiring extra water to wet their surface. This reduces the free water content in the cement  
214 pastes thereby reducing their workability. This is consistent with previous studies on cementitious

215 materials containing GO sheets [23]. The workability of the cement pastes can be tuned by adding  
216 water reducing admixtures to promote the electrostatic repulsions between the cement particles  
217 and the BNP sheets.

#### 218 *3.4. Influence of BNPs on the degree of hydration of cementitious composites*

219 The TGA results in terms of weight loss and derivative of the weight loss (DTA) are presented in  
220 Fig. 10 for the cementitious composites. In this figure, the percentage of the weight loss gradually  
221 decreases as the temperature increases and the inflections in the DTA represent the decomposition  
222 of specific phases of the cement paste composites. The TGA/DTA provides insight into the  
223 chemical reaction mechanisms in cementitious materials during heating. During this test, it was  
224 observed that C-S-H and carboaluminate phases lose their bound water in the temperature range  
225 180-300 °C; the dehydroxylation of  $\text{Ca}(\text{OH})_2$  takes place in the temperature range 430-480°C and  
226 the decarbonation of calcium carbonate ( $\text{CaCO}_3$ ) occurs in the temperature range 600–780°C.  
227 From Fig. 10, it can be observed that the mass loss of the cementitious composites decreases with  
228 increasing BNP concentration. This is due to the increase of the high density C-S-H content and  
229 the creation of new intercalated BNP/C-S-H nanocomposites with higher density. This is  
230 consistent with Rehman et al. [24] findings where they have shown that the decrease in the mass  
231 loss of GO cementitious composites is attributed to both the bonding of C-S-H with the GO sheets  
232 and the increase of the C-S-H content. In this case, the GO sheets tend to increase the amount of  
233 C-S-H product, thereby filling the pores in the matrix resulting in less amount of water available  
234 for evaporation [24].

235 The DOH is directly correlated to the amount of  $\text{Ca}(\text{OH})_2$ , which can be calculated with the method  
236 introduced by Wang et al. [25]. In this method, the mass loss in the temperature range 400-500°C  
237 divided by the final mass at 1100°C is considered as the percentage of  $\text{Ca}(\text{OH})_2$ . Figure 11 presents

238 the  $\text{Ca(OH)}_2$  content as a function of BNP concentration at 7, 14 and 28 days. At 7 and 28 days,  
239 the overall trend observed is that the amount of  $\text{Ca(OH)}_2$  increases with increasing BNP  
240 concentration. However, it is interesting to note that this trend is not evident at 14 days and this  
241 needs to be investigated further. Overall, Fig. 11 suggests that the addition of BNP sheets  
242 accelerates the hydration of cement, which results in the production of higher  $\text{Ca(OH)}_2$  contents at  
243 7 and 28 days.

244 According Cao et al. [26], the DOH can be obtained by dividing the amount of the chemically  
245 bound water (CBW) per unit gram of unhydrated cement by the CBW of fully hydrated cement  
246 which is 0.23g. The CBW can be obtained by dividing the mass loss between 140 and 1100 °C by  
247 the final mass [26]. Figure 12 shows the DOH as a function of BNP concentration at 7, 14 and 28  
248 days. As can be seen from this figure, the results clearly show that the DOH increases with  
249 increasing BPN concentration. For example, the DOH of the cement paste with 0.60-wt% BNPs  
250 is increased with respect to the plain cement paste by 6%, 7%, and 9% at 7, 14 and 18 days,  
251 respectively.

252 The improvement in the hydration of cement can be attributed to the effect of the BNP sheets on  
253 the reaction of the cement particles with water. According to Cao et al. [26], hydrophilic additives  
254 disperse well the cement particles during mixing thereby producing uniform distributions of the  
255 cement particles which results in higher DOH. Furthermore, the hydrophilic BNP sheets tend to  
256 store water molecules on their surface thus acting like internal water reservoirs thereby releasing  
257 free water for further hydration. This additional hydration further increases the amount of  $\text{Ca(OH)}_2$   
258 at 7 and 28 days. In addition, based on Cao et al. [26] hypothesis, the BNP sheets embedded into  
259 the high density C-S-H could act as water channels and transfer water from the pore solution to  
260 the un-hydrated cement cores, thus fueling the hydration of the cement particles [26].

261 *3.5. Influence of BNPs on the hydration phases of cementitious composites*

262 The XRD patterns of the cementitious composites at 7, 14 and 28 days are shown in Fig. 13. As  
263 it can be seen from this figure, typical hydration phases such as ettringite, calcium hydroxide  
264  $\text{Ca(OH)}_2$ , tricalcium silicate ( $\text{C}_3\text{S}$ ) and ( $\text{CaCO}_3$ ) are identified in all cementitious composites of all  
265 ages using the pattern fitting and Rietveld refinement techniques. This indicates that the addition of  
266 BNP sheets does not alter the type and structure of the hydration products of the cementitious. The  
267 C-S-H hydration phases are difficult to identify by XRD analysis due to the lack of crystallinity  
268 and indefinite composition. As depicted, the intensity of  $\text{Ca(OH)}_2$  increases with increasing BNP  
269 concentration at 7, 14 and 28 days. This means the addition of the BNP sheets promotes the  
270 hydration of cements thereby increasing the amount of the hydration products, which is in line  
271 with the TGA results. Previous research on GO cementitious composites also reported similar  
272 findings [25]. Another way to quantify the extent of hydration of cement as a result of BNPs is to  
273 examine the magnitude of the intensity peaks of the detected  $\text{C}_3\text{S}$  phase. From Fig. 13, it appears  
274 that the intensity peaks of  $\text{C}_3\text{S}$  decreases when the BNP sheets are present. This could be attributed  
275 to the interaction of  $\text{C}_3\text{S}$  with -OH and -R-CH<sub>2</sub>- functional groups on the surface of the BNP  
276 sheets. Phases such as  $\text{C}_3\text{S}$  tend to react with water molecules adsorbed on the surface of the BNP  
277 sheets thereby increasing the amount of hydration products.

278 Monitoring of  $\text{Ca(OH)}_2$  crystal size could shed light on the effect of BNP on the growth of C-S-H  
279 phases. The size of  $\text{Ca(OH)}_2$  was obtained from the XRD analysis using the Scherrer equation.  
280 The size of  $\text{Ca(OH)}_2$  as a function of BNP concentration at 28 days is shown in Fig. 14. From this  
281 figure, it can be observed that the addition of BNP significantly decreases the size of the  $\text{Ca(OH)}_2$   
282 particles. This can be attributed to the fact that the BNP sheets promote the growth of C-S-H, thus  
283 less space available for  $\text{Ca(OH)}_2$  to grow in size. Zheng et al. [27] found that when GO is present

284 in the matrix, the size of  $\text{Ca(OH)}_2$  becomes smaller and the content of C-S-H increases, resulting  
285 in a dense structure. It is noteworthy that the addition of 0.40-wt% BNPs and 0.60 wt% BNPs  
286 leads to a  $\text{Ca(OH)}_2$  size higher than that at 0.2 wt BNPs. This could be due to the fact that the  
287 BNP sheets tend to restack at higher concentrations which in return dampers the grow of C-S-H  
288 and allows  $\text{Ca(OH)}_2$  to grow in size. Therefore, based on this observation, it appears that the  
289 content of C-S-H reaches a maximum at 0.20-wt% BNPs at 28 days.

### 290 *3.6. Influence of BNP on the microstructure of cementitious composites*

291 The microstructure of the cementitious composites at 7, 14 and 28 days is presented in Figs.15-17.  
292 As shown, the microstructure of the plain cementitious composite at 7 days (Fig. 15a) contains  
293 unreacted cement particles as well as  $\text{Ca(OH)}_2$  cubes and seeds-like particles, presumably due to  
294 a low DOH. The addition of 0.20-wt% BNPs leads to highly dense structure with some  $\text{Ca(OH)}_2$   
295 particles embedded into the C-S-H gel (Fig. 15b). The hydration phase  $\text{Ca(OH)}_2$  in the form of  
296 cubes and rods-like crystals is observed in the microstructure of the composite with 0.40-wt%  
297 BNPs (Fig. 15c). The cementitious composite with 0.60-wt% BNPs however, is marked by a high  
298 content of  $\text{Ca(OH)}_2$  seeds like crystals (Fig. 15d). It is worth to note that it is challenging to  
299 identify the BNP sheets in the SEM images. This is because the hydration products such as  
300 ettringite,  $\text{Ca(OH)}_2$  and C-S-H grow on their surface thus making their morphology  
301 undistinguishable.

302 From Figure 16a, it can be seen that the microstructure of the plain cementitious composite at 14  
303 days becomes somewhat porous and contains a relatively high content of  $\text{Ca(OH)}_2$  seeds-like  
304 crystals, whereas the cementitious composite with 0.20-wt% BNPs (Fig. 16b) remains dense and  
305 its C-S-H content seems to increase. The cementitious composite with 0.40-Wt% BNPs exhibits  
306 a different morphology where the  $\text{Ca(OH)}_2$  seeds transformed into rods-like crystals and begin to

307 grow out from the matrix (Fig. 16c). As can be seen from Fig. 16d, when the BNP concentration  
308 increases from 0.4-wt% BNPs to 0.6-wt% BNPs, the main hydration phase of the cementitious  
309 composite is  $\text{Ca(OH)}_2$  in the form of agglomerates.

310 At 28 days of curing, the plain cementitious composite is mainly composed of  $\text{Ca(OH)}_2$  in the form  
311 of regular polyhedral shaped particles (17a). On the other hand, the cementitious composite with  
312 0.20-wt% BNPs shows a compact structure with some layers of stacked fabrics-like  $\text{Ca(OH)}_2$   
313 crystals embedded into high density C-S-H gel (Figs. 17b-c). Most of these  $\text{Ca(OH)}_2$  fabrics  
314 appear to grow in one-direction. This could be the result of the interaction of the uniformly  
315 distributed BNP sheets with the cement particles. We hypothesized that when uniformly  
316 distributed, the BNP sheets adsorb onto the surface of the cement particles through their -OH and  
317 -R-CH<sub>2</sub>- functional groups. These functional groups then react with C<sub>3</sub>S and C<sub>2</sub>S to form  
318 nucleation and growth sites for the hydration phases. The phase C<sub>2</sub>S is less soluble than C<sub>3</sub>S, thus  
319 a slower hydration rate of C<sub>2</sub>S at these growth sites. At lower BNP concentrations, this could  
320 allow more time for the hydration phases to self-assemble into fabric like-crystals. At a  
321 concentration of 0.4-wt%, the cementitious composite contains C-S-H and  $\text{Ca(OH)}_2$  as hydration  
322 products. The  $\text{Ca(OH)}_2$  particles are in the form of elliptical needles growing out from the matrix  
323 in two directions (Fig. 17d). When the BNP concentration increases to 0.6-wt% BNPs,  $\text{Ca(OH)}_2$   
324 is the main hydration product and the needle particles become cauliflower-like crystals as shown  
325 in Figs. 17e-f. The SEM investigations suggest that the BNP sheets have the ability to regulate  
326 the crystallization and morphology of the hydration products, which depends on the BNP  
327 concentration in the cement matrix. The SEM investigations also suggest that the 0.20-wt% BNP  
328 is the optimal concentration for increasing the C-S-H content in the cementitious composites.

329 The TEM images in Fig. 18 show the effect of BNP on the microstructure of the cementitious  
330 composites at 28 days. As shown, the microstructure of the plain cementitious composite mainly  
331 consists of  $\text{Ca}(\text{OH})_2$  crystals with a low C-S-H content (Fig. 18a). The addition of 0.2-wt% BNPs  
332 leads to higher C-S-H content, fewer  $\text{Ca}(\text{OH})_2$  crystals and denser microstructure (Fig. 18b). The  
333 TEM image shown in Fig. 18c confirms the existence of fabric-like crystals in the cementitious  
334 composite with 0.2-wt% BNPs. From Fig. 18d, the microstructure of the cementitious with 0.4-  
335 wt% BNPs contains  $\text{Ca}(\text{OH})_2$  crystals embedded into C-S-H gel. On the other hand, significant  
336 amount of  $\text{Ca}(\text{OH})_2$  crystals is observed in the cementitious composite with 0.6-wt% BNPs (Fig.  
337 18e). Because of the hydroxyl functional groups on their surface, the BNP sheets are covalently  
338 bonded to C-S-H and  $\text{Ca}(\text{OH})_2$  particles, thus making it challenging to identify them in the TEM  
339 images.

340 The TEM results further confirm the TGA, XRD and SEM findings that the BNP sheets accelerate  
341 the hydration of cement thus increasing both C-S-H and  $\text{Ca}(\text{OH})_2$  contents in the cementitious  
342 composites. The TEM results also confirm that the 0.20-wt% BNPs concentration produces the  
343 highest C-S-H content.

### 344 *3.7. Influence of BNP on the Mechanical properties of cementitious composites*

345 The flexural strength ( $\sigma_c$ ) and the modulus of elasticity ( $E_c$ ) of the cement prisms were calculated  
346 as [17]:

$$347 \quad \sigma_c = \frac{3Pa}{b^3} \quad (2)$$

$$348 \quad E_c = \frac{am(3l^2 - 4a^2)}{4b^4} \quad (3)$$

349 where  $l$  is the length of the prism between the supports,  $a$  is the distance between the support and  
350 the loading point,  $P$  is the maximum applied load,  $b$  is the width and thickness of the prism and,  $m$   
351 is the slope of the tangent to the straight-line portion of the load–deflection curve.

352 The effect of BNP concentration on the average flexural strength of the cementitious composites  
353 at 7, 14 and 28 days is given in Fig. 19. This figure shows that at 7 and 14 days, the addition of  
354 0.20-wt% BNPs increases the flexural strength of the cementitious composites by 23% and 20%  
355 respectively whereas, no significant increase is observed at 0.4-wt% BNPs and 0.6-wt% BNPs  
356 concentrations. At 28 days, the flexural strength is increased by about 75% and 50% at BNP  
357 concentrations of 0.20-wt% and 0.40-wt%, respectively. This increase however, significantly  
358 diminishes at 0.60-wt% BNPs.

359 Figure 20 presents the average modulus of elasticity of the cementitious composites as a function  
360 of BNP concentration at 28 days. As depicted, the modulus of elasticity follows a similar trend to  
361 that of the flexural strength at 28 days. A significant modulus of elasticity gain of about 200% is  
362 achieved at BNP concentration of 0.20-wt%. However, like the flexural strength, the modulus of  
363 elasticity diminishes at higher BNP concentrations.

364 The improvement of mechanical properties of the cementitious composites at BNP concentrations  
365 of 0.20-wt% and 0.40-wt% can be attributed to higher C-S-H content and better packing density.  
366 The diminishing of these mechanical properties at BNP concentrations higher than 0.20-wt% is  
367 probably because of the synergetic effect of the restacking of the BNP sheets and the high content  
368 of Ca(OH)<sub>2</sub> crystals. We hypothesize that at higher BNP concentrations, severe restacking of the  
369 BNP sheets occurs in the high alkaline cement pastes, thereby reducing their mechanical  
370 properties. The high alkaline cement pore solution rich in Ca<sup>2+</sup> ions attenuates the hydroxyl groups  
371 on the surface of the BNP sheets and high van-der-Waals forces are created, thereby allowing the  
372 sheets to stack on top of each other to form stiff agglomerates [17]. These agglomerates weaken  
373 the matrix, causing the cement composites to fail in a brittle manner with lower mechanical  
374 properties. The high content of Ca(OH)<sub>2</sub> crystals in the cementitious composites containing 0.40-

375 wt% BNPs and 0.60-wt% BNPs could also diminish the mechanical properties. Ca(OH)<sub>2</sub> crystals  
 376 are typically brittle in nature thereby weakening the cement matrix by making it highly susceptible  
 377 to a brittle fracture. Based on this, 0.20-wt% BNPs is the optimal content for maximum  
 378 mechanical properties.

### 379 3.8. Interaction mechanism between BNP and cement matrix

380 The improvement of the mechanical properties of the cementitious composites containing 0.20-  
 381 wt% BNPs and 0.40-wt% BNPs can be attributed both to improved hydration kinetics of the  
 382 cement particles which results in higher C-S-H content and the reinforcing effect of the BNP  
 383 sheets. The reinforcing effect is controlled by the mechanical interaction between the BNP sheets  
 384 and the cementitious matrix coupled with chemical cross-linking type bonding. As showing in  
 385 Fig. 6b, the BNP sheets are characterized by a wrinkled texture. This morphology plays a  
 386 significant role in the toughening and load transfer mechanisms in the cementitious composites,  
 387 because it enhances the mechanical interlocking [17]. Saafi et al. [17] have shown that the  
 388 mechanical interaction between the BNP sheets and the cement matrix can be examined using both  
 389 the morphology of the BNP sheets and the shear lag model. The strain  $\epsilon_p$  in the BNP sheet as a  
 390 function of the strain  $\epsilon_m$  in the cement matrix is [28]:

$$391 \quad \epsilon_p = \epsilon_m \left[ 1 - \frac{\cosh\left(\frac{nsx}{l}\right)}{\cosh\left(\frac{ns}{l}\right)} \right] \quad (4)$$

$$392 \quad n = \sqrt{\frac{2G_m t}{E_p T}}$$

393 where  $s$  is the aspect ratio of the BNP sheet ( $l/t$ ),  $n$  represents the interfacial stress transfer  
 394 efficiency and the product  $ns$  represents both the morphology of the BNP sheet and the degree of

395 interaction with the cementitious material.  $G_m$  is the shear modulus of the cementitious material,  
 396  $t$  is the thickness of the BNP sheet,  $T$  is the total thickness of the cementitious material,  $E_p$  is the  
 397 modulus elasticity of the BNP sheet and  $l$  is the length of the BNP sheet in the x direction [28].  
 398 The mechanical interaction between the two materials is slowly depending on the morphology of  
 399 the BNP sheet (Fig. 6b) which can be characterized by the wavelength  $\lambda$  and the amplitude  $A$  of  
 400 the wrinkles and ribs as [29]:

$$401 \quad \lambda^4 = \frac{4\pi^2\nu(tl)^2}{3(1-\nu^2)\varepsilon} \quad (5)$$

$$402 \quad A^2 = \left[ \frac{16\varepsilon\nu}{3\pi^2(1-\nu^2)} \right]^{\frac{1}{2}} tl \quad (6)$$

403 where  $\varepsilon$  is the compressive strain in the BNP sheet resulting from the chemical treatment,  $\nu$  is the  
 404 Poisson's ratio of the BNP sheet. The shear stress  $\tau$  between the BNP sheet and the matrix in the  
 405 direction  $x$  is [29]:

$$406 \quad \tau = nE_p\varepsilon_m \frac{\sinh\left(\frac{nsx}{l}\right)}{\cosh\left(\frac{ns}{2}\right)} \quad (7)$$

407 Equations (4), (5), (6) and (7) indicate that the observed increase in the mechanical properties of  
 408 the BNP cementitious composites at 0.20-wt% BNPs and 0.40-wt% BNPs is in part as a result of  
 409 a good mechanical interaction between the two materials which is controlled by properties of the  
 410 BNP sheets mainly the high aspect ratio, the modulus of elasticity and the surface morphology.

411 The BNP characterization results indicate that the BNP sheets are fully decorated with hydroxyl  
 412 functional groups which are responsible for their high chemical reactivity. These functional  
 413 groups are believed to adsorb on the surface of the cement particles. In this case, the main chemical  
 414 components of the cement  $C_2S$  and  $C_3S$  hydrate over the surface of the BNP sheets, leading to

415 intercalated C-S-H/BNP and  $\text{Ca}(\text{OH})_2$ /BNP particles. Figure 21 shows the chemical interaction  
416 of the BNP sheets with C-S-H at 28 days. The strong interfacial covalent bonding between C-S-  
417 H and the functionalized BNP sheets enhances the stress transfer thus improving the overall  
418 mechanical properties of the cementitious composites at BNP concentrations of 0.20-wt% and  
419 0.40-wt%.

420 As shown in Figs 22 and 23, the maximum percentage increase in the flexural strength of the BNP-  
421 cementitious composite at 0.20-wt% is compared with that of several cementitious composites  
422 containing MWCNT and GO obtained from [30-47]. As shown in these figures, overall, the BNP  
423 outperforms MWCNTs and GO. This is due to high dispersibility of the BNP flakes in the cement  
424 paste. In addition, the BNP flakes contains more hydroxyl groups, thus better chemical reactivity  
425 which improves the hydration of cement.

### 426 *3.9. Influence of BNP on the Fracture properties of cementitious composites: numerical simulation* 427 *and experimental results*

428 The three-point-bending fracture tests were numerically simulated by ABAQUS to further  
429 elucidate their fracture behavior and validate the experimental results. In order to capture the  
430 evolution of cracks, extended finite element method (X-FEM) was used as the finite element mesh  
431 need not conform to the varying internal boundaries caused by the propagation of cracks. Hence,  
432 a single mesh is sufficient for completing entire simulation of a test. Fig.24 shows the geometry  
433 of the X-FEM model for the cement prism with and without BNP. The dimensions of the prisms  
434 are identical to the ones used in the laboratory tests. The prisms are simply supported near the two  
435 ends. The force is applied at the mid-span, where a 16mm long virtual crack perpendicular to the  
436 bottom surface is embedded. The prisms were discretized by cubic C3D8R elements. Mesh  
437 sensitivity analysis was carried out and it was found that elements of  $2\text{mm}\times 2\text{mm}\times 2\text{mm}$  were

438 sufficiently small to achieve converged results. The maximum principal stress fracture criteria  
439 was used to initiate fracture. The material properties of the cementitious composites of the XFEM  
440 models were taken from the laboratory tests described in Sections 3.7 and 3.8 and, the details are  
441 shown in Table 2.

442 Figure 25 shows the predicted and measured load vs CMOD response plain prisms and prisms  
443 with 0.20-wt% BNPs (optimal BNP concentration). It is worth mentioning that it was not possible  
444 to experimentally capture the post-cracking response of the prisms due to the limitation of the test  
445 machine employed in this investigation. As shown, at the optimal BNP concentration, the fracture  
446 load, stiffness and the amount of absorbed energy are significantly increased, thus better fracture  
447 properties. Figure 25 shows that the FEM model provides a good prediction of the fracture load  
448 of the prisms, though it overestimates their stiffness.

449 The experimental fracture energy  $G_f$  and the fracture toughness  $K_{IC}$  were calculated according to  
450 [48]. The calculated average  $G_f$  and  $K_{IC}$  are about 12.55 Nm/m<sup>2</sup>, 0.16 MPa m<sup>0.5</sup>, respectively, for  
451 the plain prism, and 23.61 Nm/m<sup>2</sup> and 0.33 MPa m<sup>0.5</sup> respectively, for the prism containing 0.20-  
452 wt% BNPs. This shows that the addition of BNPs increases  $G_f$  and  $K_{IC}$  by about 88% and 106%,  
453 respectively.

454 Figure 26 compares the observed and simulated cracking behavior of the prisms. As shown, there  
455 is a good agreement between both the simulated and experimental failure mode of the prisms. The  
456 failure mode of the plain cement prism is Mode I crack propagation along the surface of the initial  
457 notch. The failure mode of the prism containing 0.20-wt% BNPs is somewhat mixed mode (Mode  
458 I+II) crack propagation in the form of an inclined crack initiated slightly above the notch tip. This  
459 can be attributed to the BNP crack deflection effect and the improved flexural strength.

460 The significant increase in the fracture properties of the BNP cementitious composites is attributed  
461 to the toughening mechanisms originated from the presence of BNP sheets. As shown in Fig. 27b,  
462 the toughness seems to be governed by the crack-bridging mechanism where the BNP sheet  
463 appears to disentangle into nanofibers under stress and bridge the crack. Figures 27c and 27d show  
464 another toughening mechanism associated with mainly crack deflection that bypasses the BNP  
465 sheet at the BNP/matrix interface.

## 466 **Conclusions**

467 In this paper, we demonstrate for the first time that nanoplatelets synthesized from food waste such  
468 as sugar beetroot can be used as a low-cost and renewable reinforcing material in cementitious  
469 materials. The proposed BNP sheets exhibit some characteristics of GO such as hydrophilic  
470 functional groups, high specific area and good dispersibility in water. An integrated experimental  
471 and numerical simulation approach was employed to evaluate the performance of cementitious  
472 composites containing BNP sheets.

473 Because of their high surface area and hydrophilicity, the BNP sheets tend to consume water  
474 thereby reducing the workability of the cement pastes at BNP concentrations higher than 0.20-  
475 wt%. The incorporation of the BNP sheets increased the degree of hydration of cement due to the  
476 active participation of their functional groups and their supply of water molecules, resulting in  
477 high content of the hydration products. The microstructure, the type of the hydration phases and  
478 the mechanical properties seemed to be highly dependent on the amount of the BNP sheets.  
479 Compared to the plain cementitious composite, the cementitious composite with 0.20-wt% BNPs  
480 showed a microstructure with better packing density with C-S-H as the main hydration phase. At  
481 higher BNP concentrations,  $\text{Ca(OH)}_2$  was the main hydration phase. The BNP sheets appeared to  
482 regulate the morphology of  $\text{Ca(OH)}_2$  crystals. At 28 days, the regular polyhedral shaped  $\text{Ca(OH)}_2$

483 particles in the plain cementitious composite changed to stacked fabric-like  $\text{Ca(OH)}_2$  at 0.20-wt%  
484 BNPs, elliptical needles at 0.40-wt% BNPs and cauliflower-like  $\text{Ca(OH)}_2$  at 0.60-wt%.

485 The experimental results suggested that 0.20-wt% BNPs is the optimal concentration for maximum  
486 amount of C-S-H gel and mechanical properties. At this BNP content, the flexural strength and  
487 the modulus of elasticity were by increased by 75% and 200%, respectively due to a good packing  
488 density of the cement paste. However, these mechanical properties diminished at higher BNP  
489 concentrations due to restacking of BNP and increased amount of  $\text{Ca(OH)}_2$ . Both experimental  
490 and numerical simulation results showed that the fracture resistance of the cementitious  
491 composites were significantly improved at 0.20-wt% BNPs due to the crack bridging and crack  
492 deflection effects of the BNP sheets. At this concentration, the fracture energy and the fracture  
493 toughness were increased by about 88% and 106%, respectively.

494 Although further studies are required to investigate the durability of the proposed cementitious  
495 composites and optimize their properties, the proposed 2D BNP has the potential to create durable  
496 and high performance cementitious materials with low-embodied carbon for various applications  
497 in the construction sector.

#### 498 **Acknowledgements**

499 The authors would like to acknowledge the financial support H2020-MSCA-IF under the grant  
500 No. 799658\_B-SMART: Biomaterials derived from food waste as a green route for the design of  
501 eco-friendly, smart and high performance cementitious composites for the next built infrastructure.

502 The authors would like to thank the Iraqi Government for providing a PhD scholarship to the first  
503 author. The authors are grateful for Cellucomp Ltd for providing the BNP material.

504

505

506 **References**

- 507 [1] Y. Reches, Nanoparticles as concrete additives: Review and perspectives, *Construction and*  
508 *Building Materials* 175 (2018) 483-495.
- 509 [2] F. Sanchez, K. Sobolev Nanotechnology in concrete—a review, *Construction and building*  
510 *materials* 397 24(11) (2010) 2060-2071.
- 511 [3] T. Ji, Preliminary study on the water permeability and microstructure of concrete incorporating  
512 nano-SiO<sub>2</sub>. *Cement and Concrete Research*. 2005;35(10):1943-7.
- 513 [4] H. Li, H.G. Xiao, J. Yuan, J. Ou, Microstructure of cement mortar with nano-particles.  
514 *Composites Part B: Engineering*. 2004;35(2):185-9.
- 515 [5] H. Li, H. Xiao, X. Guan, Z. Wang, L. Yu, Chloride diffusion in concrete containing nano-TiO  
516 <sub>2</sub> under coupled effect of scouring. *Composites Part B: Engineering*. 2014;56:698-704.
- 517 [6] L. Senff, D. Tobaldi, S. Lucas, D. Hotza, V. Ferreira, J. Labrincha, Formulation of mortars  
518 with nano-SiO<sub>2</sub> and nano-TiO<sub>2</sub> for degradation of pollutants in buildings. *Composites Part B:*  
519 *Engineering*. 2013;44(1):40-7.
- 520 [7] S. Kawashima, JWT. Seo, D. Corr, MC. Hersam, SP. Shah, Dispersion of CaCO<sub>3</sub>  
521 nanoparticles by sonication and surfactant treatment for application in fly ash–cement systems.  
522 *Materials and structures*. 2014;47(6):1011-23.
- 523 [8] W. Li, Z. Huang, T. Zu, C. Shi, WH. Duan, SP. Shah, Influence of nanolimestone on the  
524 hydration, mechanical strength, and autogenous shrinkage of ultrahigh-performance concrete.  
525 *Journal of Materials in Civil Engineering*. 2015;28(1):04015068.
- 526 [9] Z. Pan, L. He, L. Qiu, AH. Korayem, G. Li, JW. Zhu, et al., Mechanical properties and  
527 microstructure of a graphene oxide–cement composite. *Cement and Concrete Composites*. 2015;  
528 58:140-7.

529 [10] BM. Tyson, Abu Al-Rub RK, Yazdanbakhsh A, Grasley Z, Carbon nanotubes and carbon  
530 526 nanofibers for enhancing the mechanical properties of nanocomposite cementitious materials.  
531 Journal of Materials in Civil Engineering. 2011;23(7):1028-35.

532 [11] A, Cwirzen, K. Habermehl-Cwirzen, A. Nasibulin, E. Kaupinen, P. Mudimela, V. Penttala,  
533 SEM/AFM studies of cementitious binder modified by MWCNT and nano-sized Fe needles.  
534 Materials Characterization. 2009;60 (7):735-40.

535 [12] Y. Xu, J. Zeng, W. Chen, R. Jin, B. Li, Z. Pan, A holistic review of cement composites  
536 reinforced with graphene oxide, Construction and Building Materials 171 (2018) 291-302.

537 [13] S. Lv, Y. Ma, C. Qiu, T. Sun, J. Liu, Q. Zhou, Effect of graphene oxide nanosheets of  
538 microstructure and mechanical properties of cement composites, Constr. Build. Mater. 49 (2013)  
539 121–127. doi:10.1016/j.conbuildmat.2013.08.022.

540 [14] M.M. Mokhtar, S.A. Abo-El-Enein, M.Y. Hassaan, M.S. Morsy, M.H. Khalil, Mechanical  
541 performance, pore structure and micro-structural characteristics of graphene oxide nano platelets  
542 reinforced cement, Construction Building Materials 138 (2017) 333–339.  
543 doi:10.1016/j.conbuildmat.2017.02.021.

544 [15] X. Li, A.H. Korayem, C. Li, Y. Liu, H. He, J.G. Sanjayan, W.H. Duan, Incorporation of  
545 graphene oxide and silica fume into cement paste: A study of dispersion and compressive strength,  
546 Construction and Building Materials 123 (2016) 327-335.

547 [16] K. Gong, Z. Pan, A.H. Korayem, L. Qiu, D. Li, F. Collins, C.M. Wang, W.H. Duan.  
548 Reinforcing Effects of Graphene Oxide on Portland Cement Paste, J. Mater. Civ. Eng. 27 (2015)  
549 A4014010. doi:10.1061/(ASCE)MT.1943-5533.0001125.

550 [17] M. Saafi, L. Tang, J. Fung, M. Rahman, J. Liggat, Enhanced properties of graphene/fly ash  
551 geopolymetric composite cement, *Cem. Concr. Res.* 67 (2015) 292–299,  
552 doi:10.1016/j.cemconres.2014.08.011.

553 [18] B. Wang, R. Jiang 1, Z. Wu, Investigation of the mechanical properties and microstructure of  
554 graphene nanoplatelet-cement composite, *Nanomaterials*, 2016, 6 (11), 200;  
555 doi:10.3390/nano6110200.

556 [19] USA Patent No: 9,834,664, Cellucomp Limited, Fife, UK.

557 [20] F. Collins, J. Lambert, W. H. Duan, The influences of admixtures on the dispersion,  
558 workability, and strength of carbon nanotube–OPC paste mixtures, *Cement & Concrete*  
559 *Composites*, 2012, 34, 201–2017, doi: 10.1016/j.cemconcomp.2011.09.013.

560 [21] Y. Cao, P. Zaverri, J. Youngblood, R. Moon, J. Weiss, The influence of cellulose  
561 nanocrystal additions on the performance of cement paste, *Cement & Concrete Composites*, 2015  
562 ,56, 73–83, doi:10.1016/j.cemconcomp.2014.11.008.

563 [22] M. Lia, L. Wang, D. Lia, YL. Cheng, B. Adhikari, Preparation and characterization of  
564 cellulose nanofibers from de-pectinated sugar beet pulp, *Carbohydrate Polymers* 102 (2014) 136–  
565 143, doi:10.1016/j.carbpol.2013.11.021.

566 [23] X. Li, YM. Liu, WG. Li, CY. Li, JG. Sanjayan , WH. Duan, Z. Li, Effects of graphene oxide  
567 agglomerates on workability, hydration, microstructure and compressive strength of cement paste,  
568 *Construction and Building Materials* 145 (2017) 402–410, doi:  
569 10.1016/j.conbuildmat.2017.04.058.

570 [24] SK. Rehman, Z. Ibrahim, SA. Memon, MdT. Aunkor, MF. Javed, K. Mehmood, SM A. Shah,  
571 Influence of graphene nanosheets on rheology, microstructure, strength development and self-

572 sensing properties of cement based composites, *Sustainability* 2018, 10(3), 822; doi:  
573 10.3390/su10030822.

574 [25] L. Wang, S. Zhang, D. Zheng, H. Yang, H. Cui, W. Tang, D. Li, Effect of graphene oxide  
575 (GO) on the morphology and microstructure of cement hydration products, *Nanomaterials* (Basel).  
576 2017 Dec 5;7(12). pii: E429. doi: 10.3390/nano7120429.

577 [26] Y. Cao, P. Zaverri, J. Youngblood, R. Moon, J. Weiss, The influence of cellulose  
578 nanocrystal additions on the performance of cement paste, *Cement & Concrete Composites* 56  
579 (2015) 73–83, doi: 10.1016/j.cemconcomp.2014.11.008.

580 [27] Q. Zheng, B. Han, X. Cui, X. Yu, J. Ou, Graphene-engineered cementitious composites: Small  
581 makes a big impact, *Nanomaterials and Nanotechnology*, Volume 7 (2017): 1–18, doi:  
582 10.1177/1847980417742304.

583 [28] L. Gong, I.A. Kinloch, R.J. Young, I. Riaz, R. Jalil, K.S. Novoselov, Interfacial stress transfer  
584 in a graphene monolayer nanocomposite, *Adv. Mater.* 22 (24) (2010), 2694–2697.

585 [29] L. Tapasztó, T. Dumitrica, S. Jin-Kim, P. Nemes-Incze, C. Hwang, L.P. Biró, Break-down of  
586 continuum mechanics for nanometer-wavelength rippling of graphene, *Nat. Phys.* 8 (2012) 739–  
587 741.

588 [30] Tyson, B. M., Abu Al-Rub, R. K., Yazdanbakhsh, A. & Grasley, Z. 2011. Carbon Nanotubes  
589 and Carbon Nanofibers for Enhancing the Mechanical Properties of Nanocomposite Cementitious  
590 Materials.(Author Abstract)(Report). *Journal of Materials in Civil Engineering*, 23(7), 1028.

591 [31] Luo, J., Duan, Z. & Li, H. 2009. The Influence of Surfactants on the Processing of Multi-  
592 Walled Carbon Nanotubes in Reinforced Cement Matrix Composites. *physica status solidi* (a), 206  
593 (12), 2783-2790.

594 [32] Metaxa, Z. S., Konsta-Gdoutos, M. S. & Shah, S. P. 2012a. Carbon Nanofiber Cementitious  
595 Composites: Effect of Debulking Procedure on Dispersion and Reinforcing Efficiency. *Cement*  
596 *and Concrete Composites*, 36(1).

597 [33] Xu, S., Liu, J. & Li, Q. 2015. Mechanical Properties and Microstructure of Multi- Walled  
598 Carbon Nanotube-Reinforced Cement Paste. *Construction and Building Materials*, 76, 16-23.

599 [34] Li, G., Wang, P, Zhao, X. 2005. Mechanical behavior and microstructure of cement  
600 composites incorporating surface-treated multi-walled carbon nanotubes. *Carbon*. 43, 1239-1245.

601 [35] Cwirzen. A, Habermehl Cwirzen. K and Penttala. V “Surface decoration of carbon nanotubes  
602 and mechanical properties of cement/carbon Nanotube composites” in *Advances in Cement*  
603 *Research*, 2008, 20, No. 2, April, pp.65–73.

604 [36] Musso, S., Tulliani, J.-M., Ferro, G. & Tagliaferro, A. 2009. Influence of Carbon Nanotubes  
605 Structure on the Mechanical Behavior of Cement Composites. *Composites Science and*  
606 *Technology*, 69(11), 1985-1990.

607 [37] Konsta-Gdoutos, M. S., Metaxa, Z. S. & Shah, S. P. 2010. Highly Dispersed Carbon Nanotube  
608 Reinforced Cement Based Materials. *Cement and Concrete Research*, 40(7), 1052-1059.

609 [38] Chan, L. Y. & Andrawes, B. 2010. Finite Element Analysis of Carbon Nanotube/Cement  
610 Composite with Degraded Bond Strength. *Computational Materials Science*, 47(4), 994-1004.

611 [39] Metaxa, Z. S., Seo, J.-W. T., Konsta-Gdoutos, M. S., Hersam, M. C. & Shah, S. P. 2012b.  
612 Highly Concentrated Carbon Nanotube Admixture for Nano-Fiber Reinforced Cementitious  
613 Materials. *Cement and Concrete Composites*, 34(5), 612-617.

614 [40] Lv, S., Liu, J., Sun, T., Ma, Y. & Zhou, Q. 2014a. Effect of Go Nanosheets on Shapes of  
615 Cement Hydration Crystals and Their Formation Process. *Construction and Building Materials*,  
616 64, 231-239.

- 617 [41] Lv, S., Ting, S., Liu, J. & Zhou, Q. 2014b. Use of Graphene Oxide Nanosheets to Regulate  
618 the Microstructure of Hardened Cement Paste to Increase Its Strength and Toughness.  
619 CrystEngComm, 16(36), 8508-8516.
- 620 [42] Lv, S., Ma, Y., Qiu, C., Sun, T., Liu, J. & Zhou, Q. 2013. Effect of Graphene Oxide  
621 Nanosheets of Microstructure and Mechanical Properties of Cement Composites. Construction and  
622 Building Materials, 49, 121-127.
- 623 [43] Shang, Y., Zhang, D., Yang, C., Liu, Y. & Liu, Y. 2015. Effect of Graphene Oxide on the  
624 Rheological Properties of Cement Pastes. Construction And Building Materials, 96, 20-28.
- 625 [44] Li, X., Liu, Y. M., Li, W. G., Li, C. Y., Sanjayan, J. G., Duan, W. H. & Li, Z. 2017. Effects  
626 of Graphene Oxide Agglomerates on Workability, Hydration,
- 627 [45] Zhou, C., Li, F., Hu, J., Ren, M., Wei, J. & Yu, Q. 2017. Enhanced Mechanical Properties of  
628 Cement Paste by Hybrid Graphene Oxide/Carbon Nanotubes. Construction and Building  
629 Materials, 134, 336-345.
- 630 [46] Muhit B. A., 2015 Investigation on the Mechanical, Microstructural, and Electrical Properties  
631 of Graphene OxideCement Composite. Master thesis, University of Central Florida.
- 632 [47] Zhao, L., Guo, X., Liu, Y., Ge, C., Guo, L., Shu, X. & Liu, J. 2017. Synergistic Effects of  
633 Silica Nanoparticles/Polycarboxylate Superplasticizer Modified Graphene Oxide on Mechanical  
634 Behavior and Hydration Process of Cement Composites. RSC Adv., 7(27), 16688-16702.
- 635 [48] Y. Hu, D. Luo, P. Li, Q. Li., G. Sun, Fracture toughness enhancement of cement paste with  
636 multi-walled carbon nanotubes, Construction and Building Materials 70 (2014), 332-338.

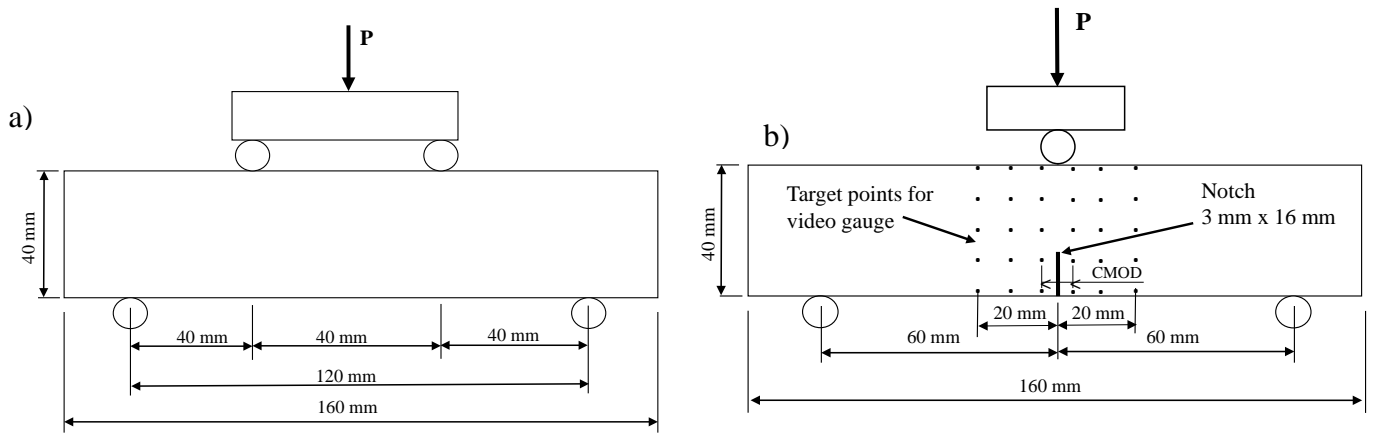


Fig. 1. Test details of the prisms and schematic of test setups. a) flexural strength test setup, b) fracture test setup (not to scale).

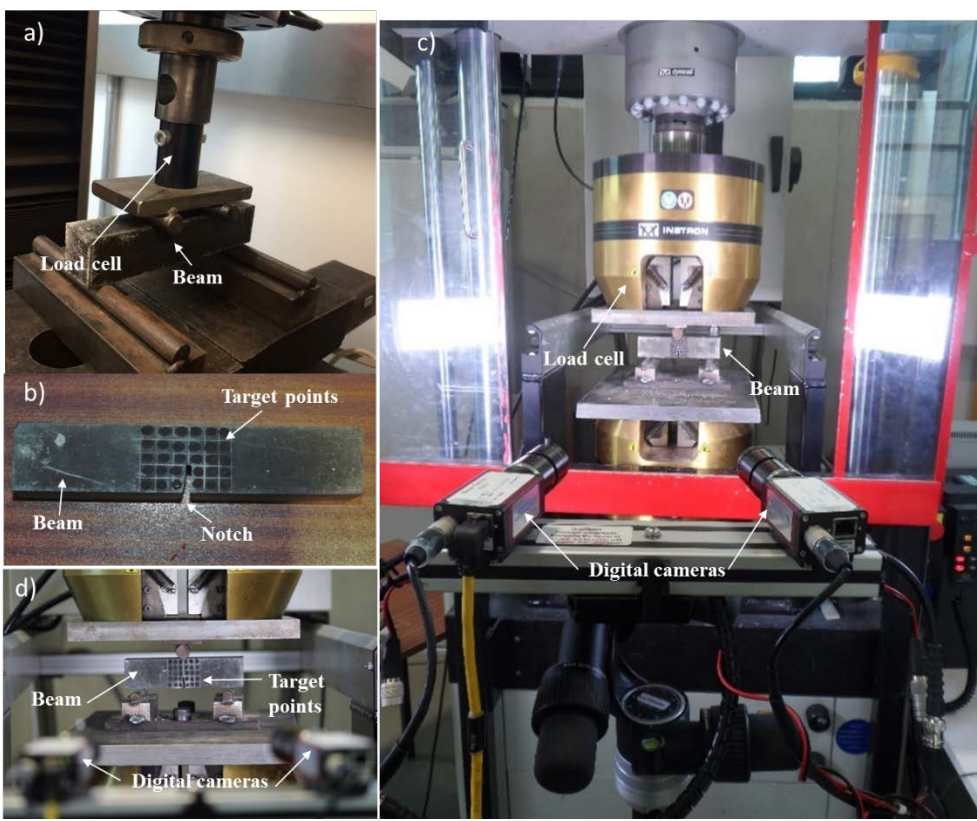


Fig. 2. Images of the experimental test setups. a) flexural strength test setup, b) notched prism with optical grid for fracture test., c) fracture test setup with digital camera for CMOD measurement, d) close up view of the notched prism under load.

Table 1: Chemicals composition of the BNP sheets

Chemical components	C	O	Ca	Al	Cl	Mg	Si	Na
Content (%)	47.6	46.9	1.9	1.8	0.7	0.5	0.4	0.2

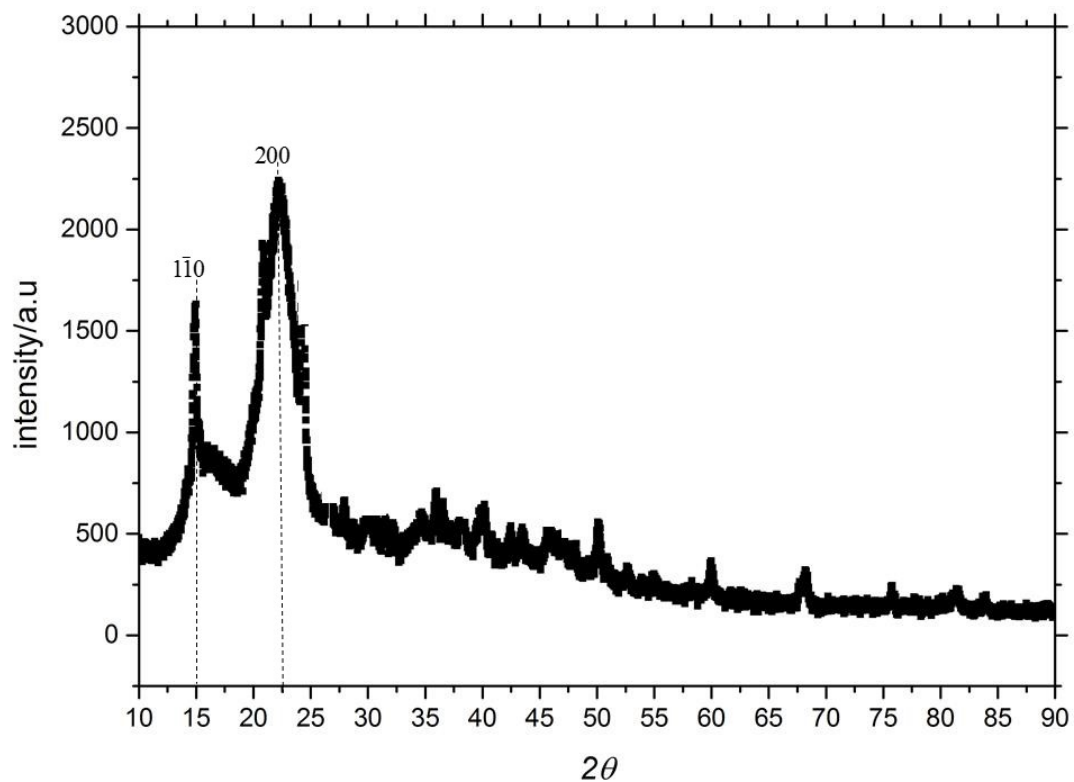


Fig. 3. XRD spectrum of the BNP sheets showing crystalline region at  $2\theta = 15$  and amorphous/crystalline regions at  $2\theta = 22.5$ .

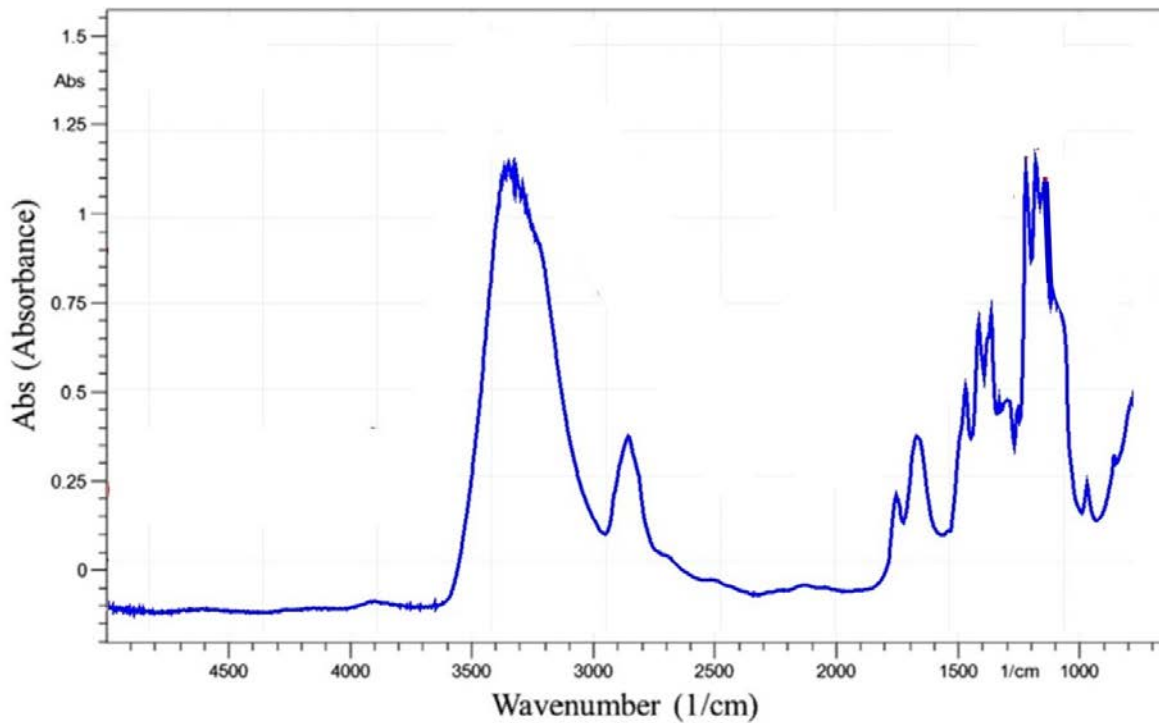


Fig. 4. Diffuse FTIR spectra of the BNP sheets used to determine the their functional groups

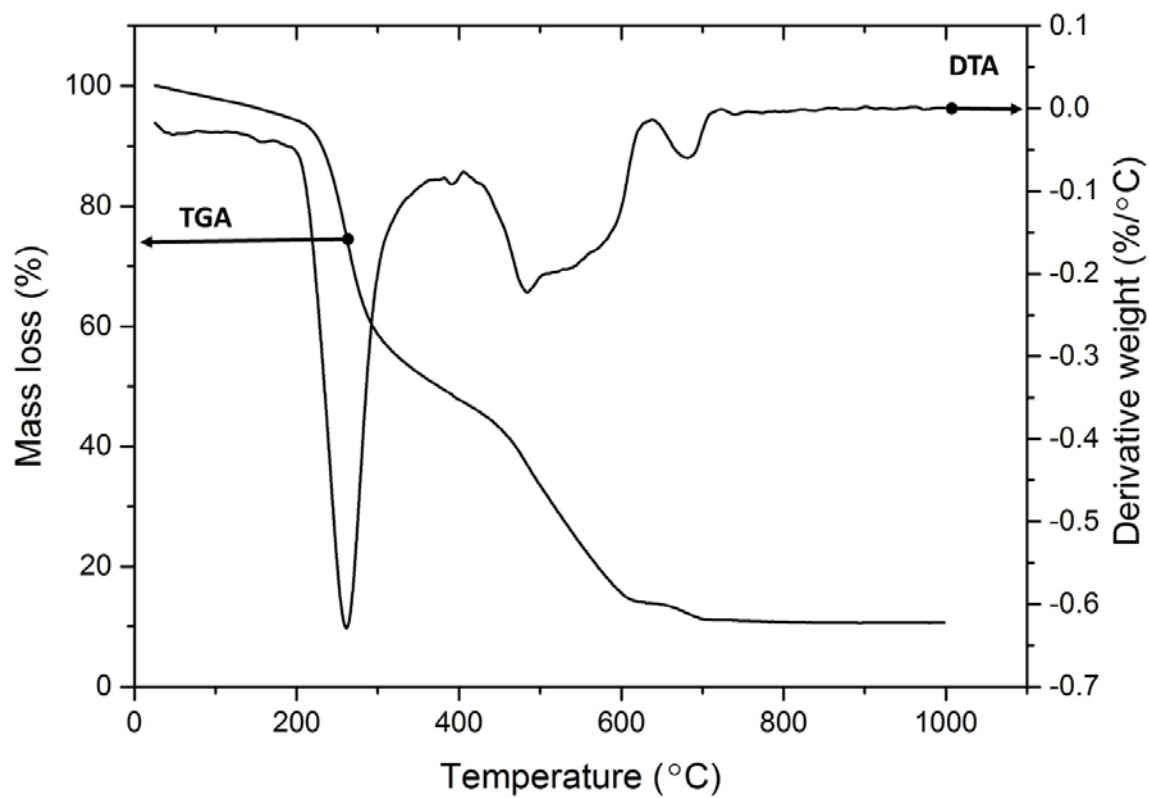


Fig. 5: Thermal stability of the BNP sheets showing TGA and DTA curves

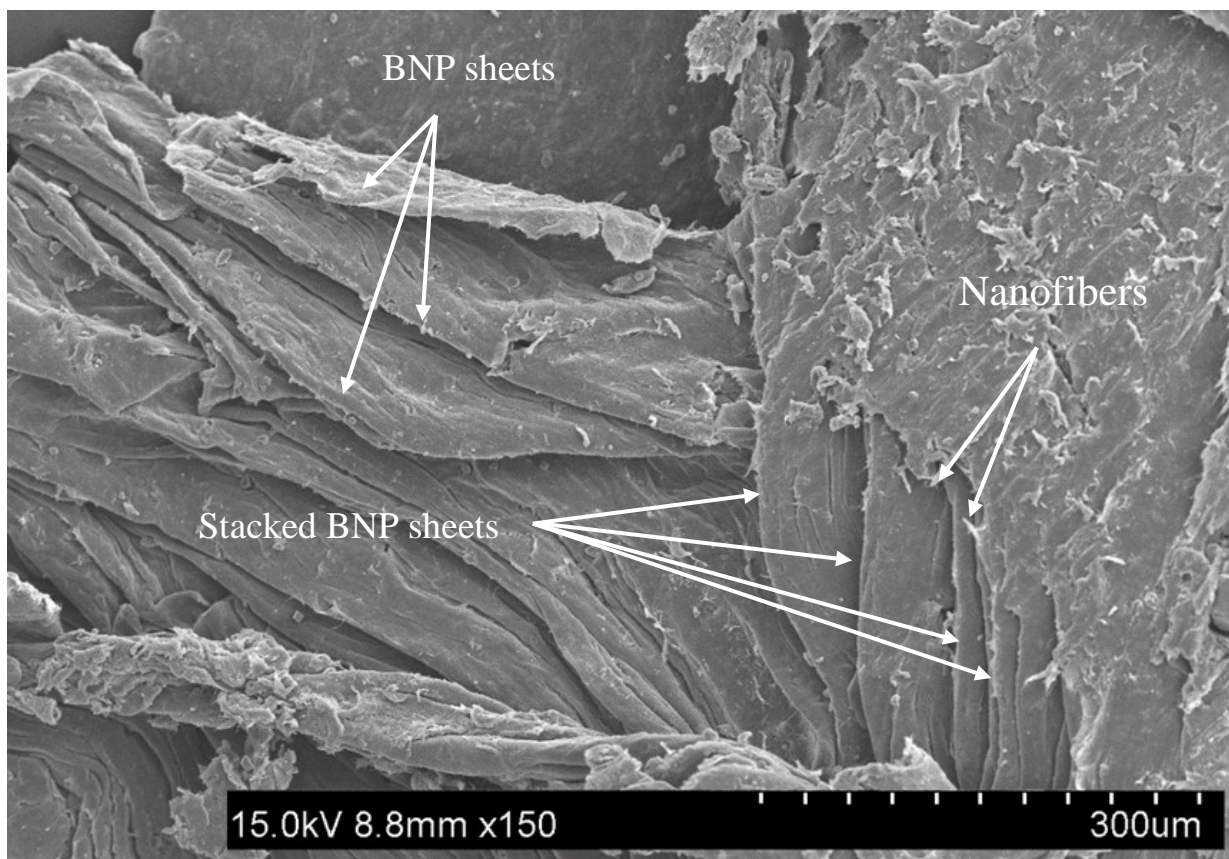


Fig. 6. SEM image showing the surface morphology of the BNP sheets.

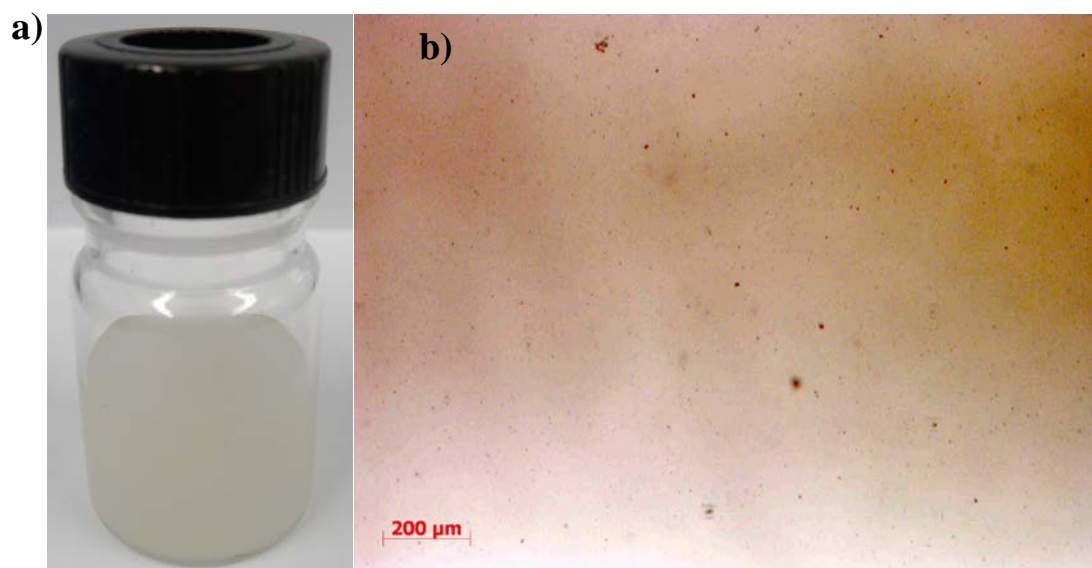


Fig. 7: a) BNP aqueous solution (2g/L) after 30 min of sonication, b) optical image of the BNP aqueous solution.

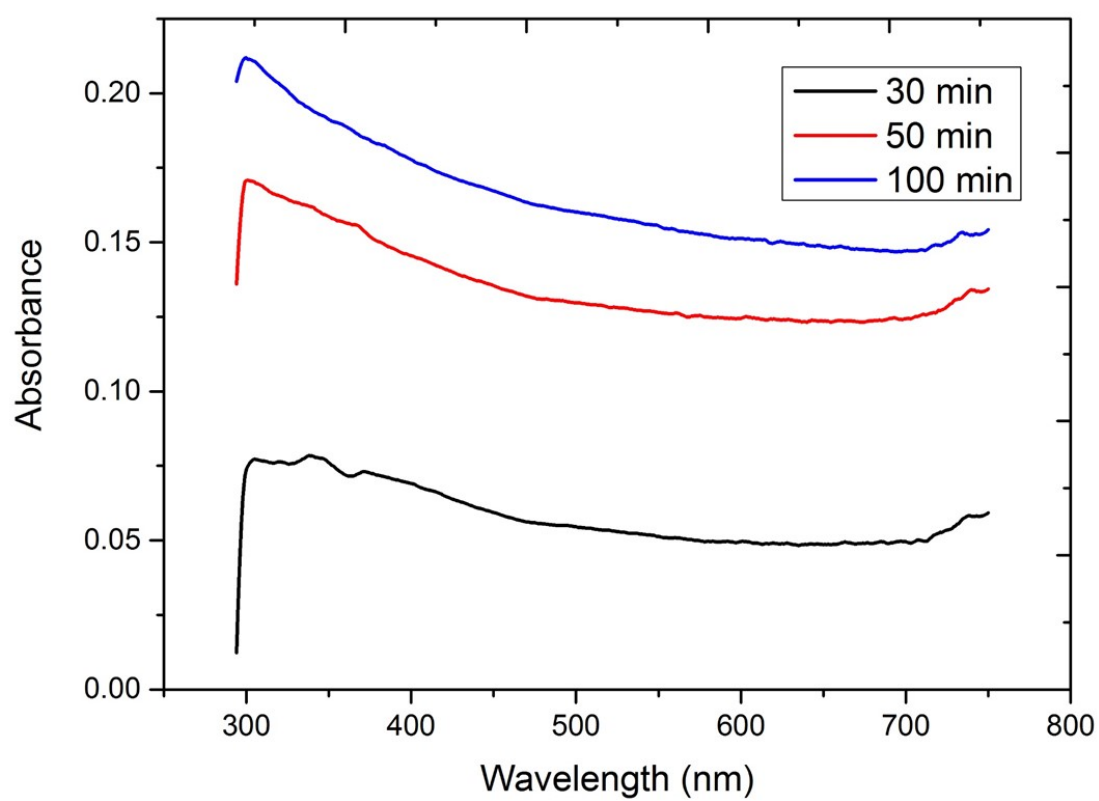


Fig.8. UV-vis spectroscopy results of BNP aqueous solutions at different sonication times

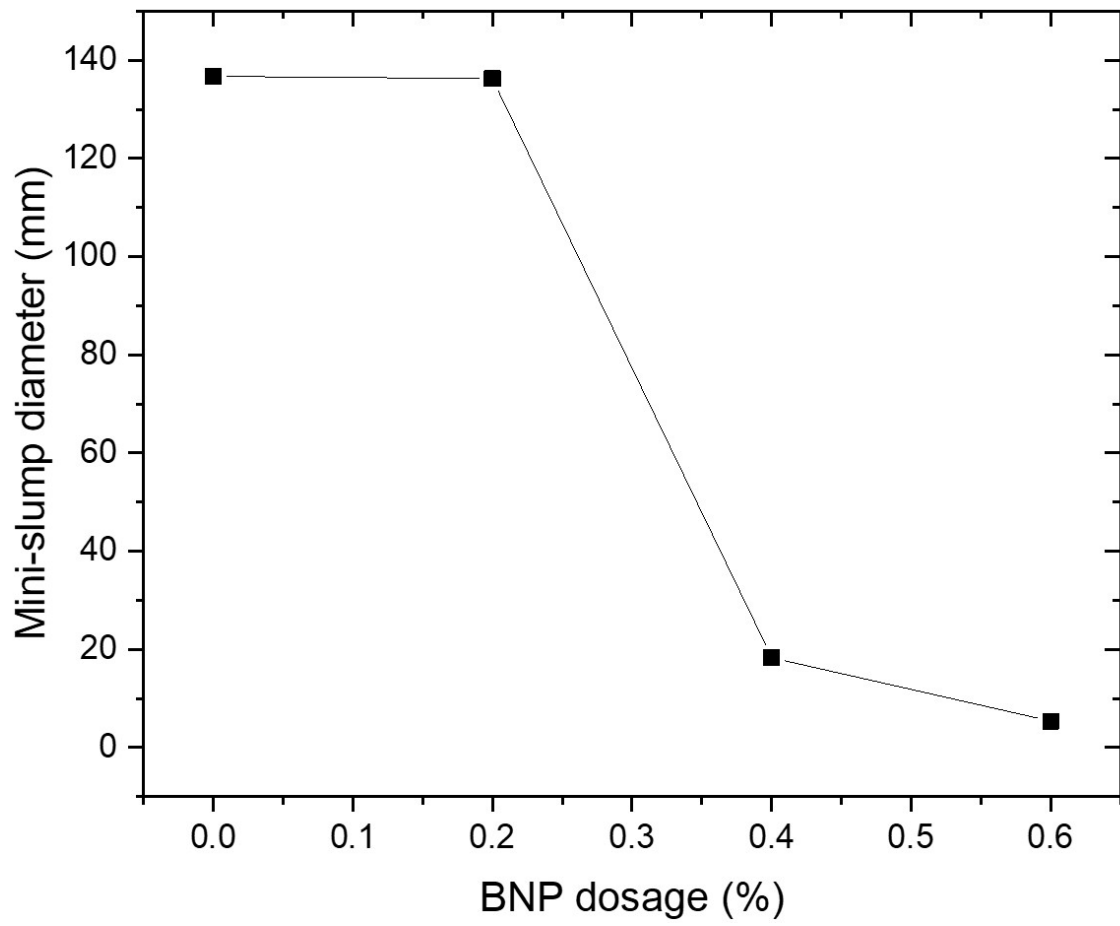


Fig. 9. Effect of the BNP sheets on the workability of the cement paste

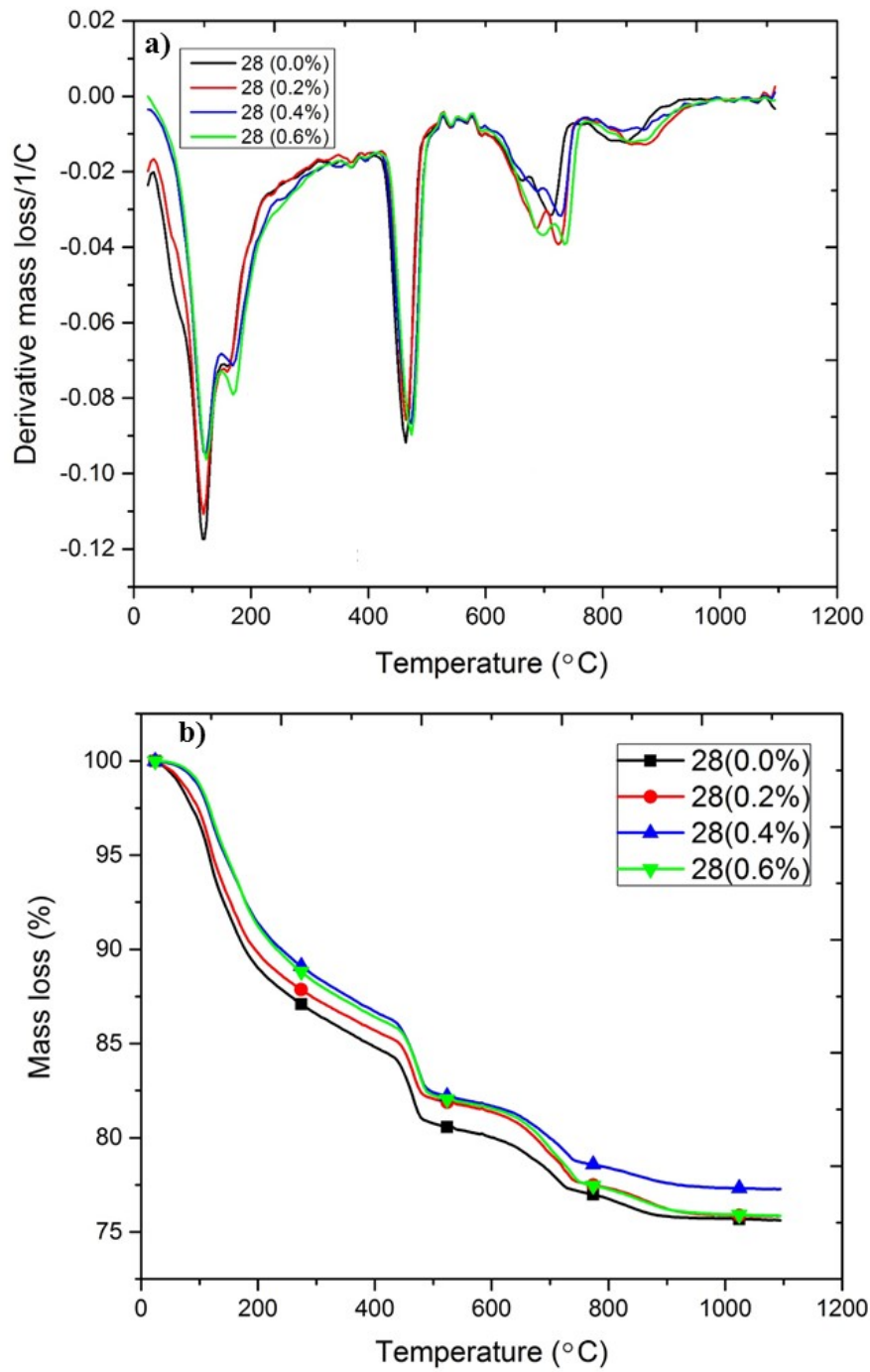


Fig. 10: TGA curves (a) and DTA curves (b) for the cementitious composites at BNP concentrations of 0 (control), 0.2, 0.4 and 0.6-wt% at 28 days.

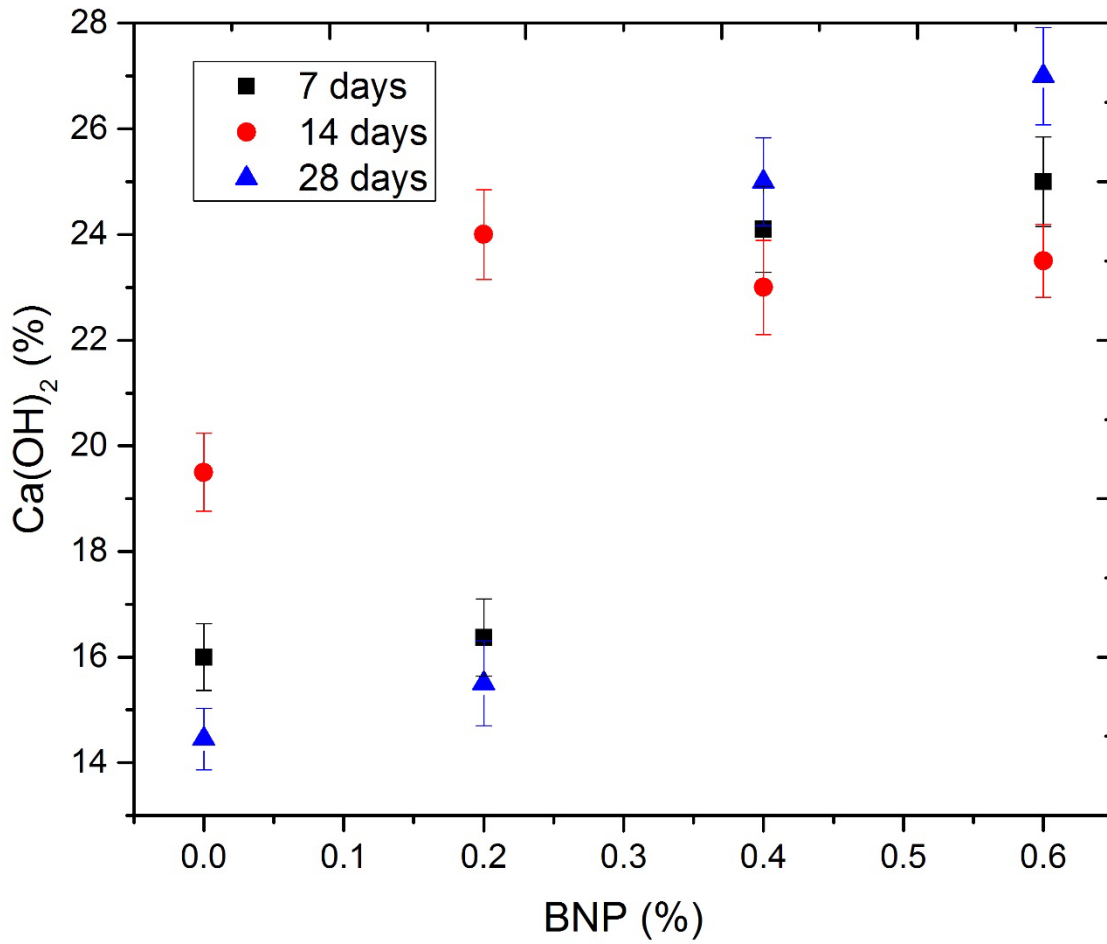


Fig. 11: Content of calcium hydroxide obtained from TGA as a function of BNP concentration at 7, 14 and 28 days

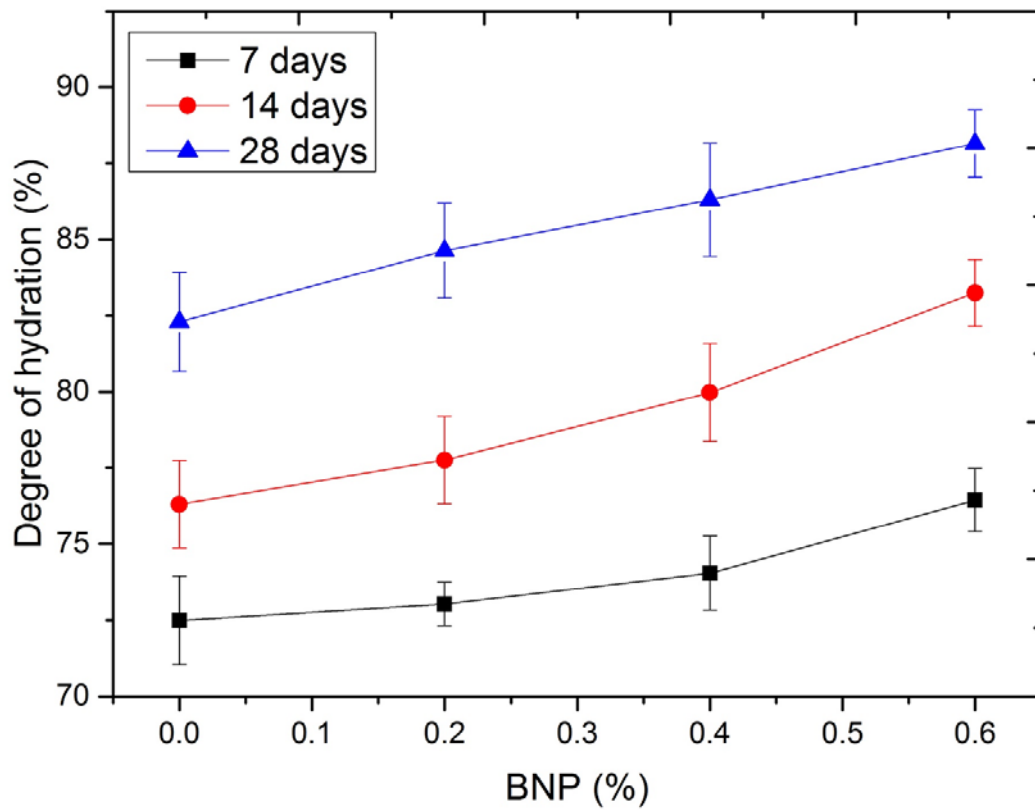


Fig. 12. Degree of hydration (DOH) of the cementitious composites obtained from TGA as a function of BNP concentration at 7, 14 and 28 days.

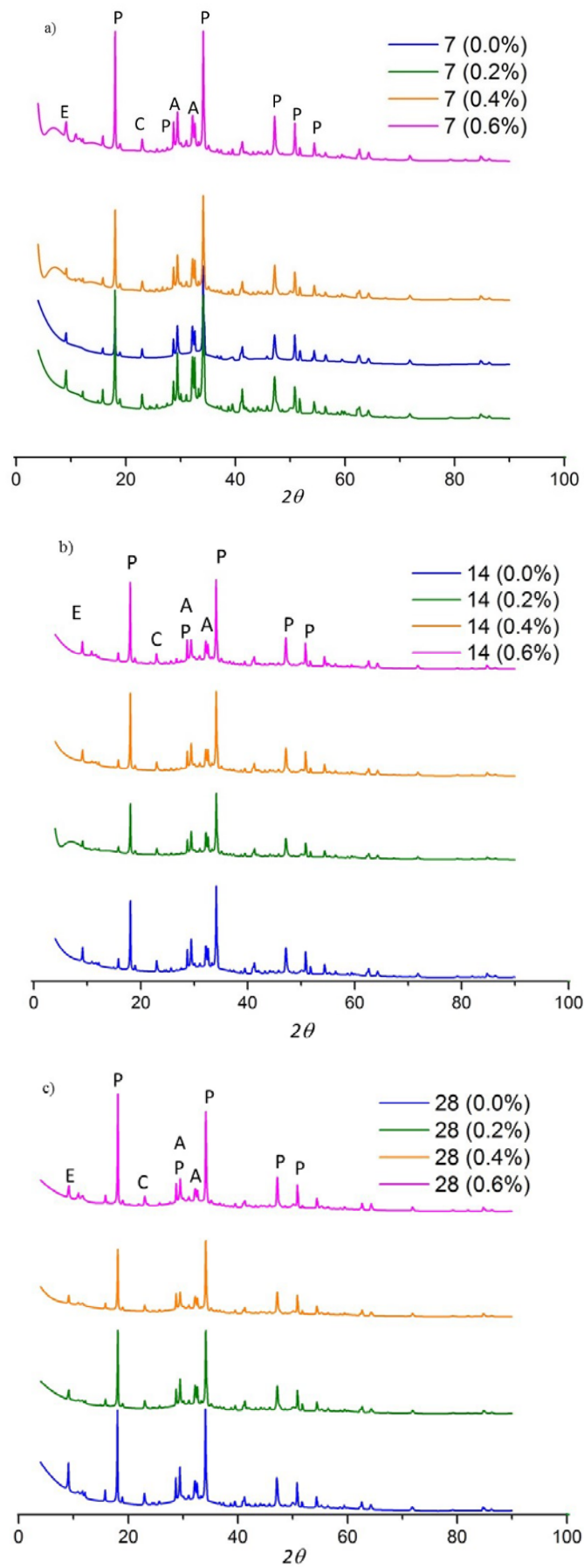


Fig. 13. XRD spectrum of the cementitious composites at different BNP concentrations, a) 7 days, b) 14 days, c) at 28 days. C-S-H: Calcium Silicate hydrate. E: Ettringite, P: Portlandite ( $\text{Ca}(\text{OH})_2$ ), A: Alite ( $\text{C}_3\text{S}$ ), C: Calcite ( $\text{CaCO}_3$ ).

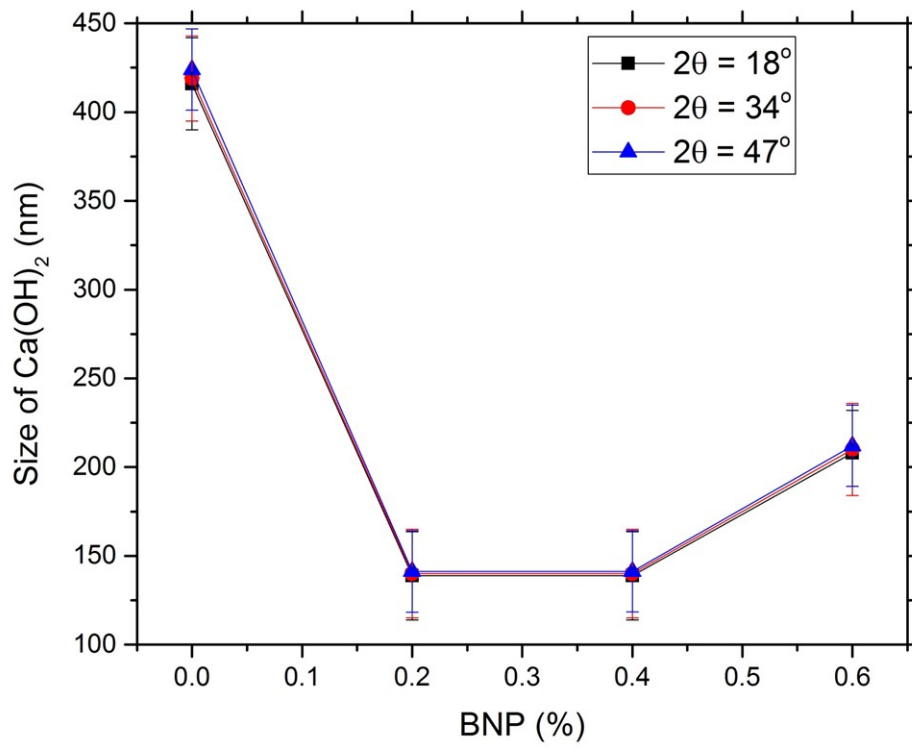


Fig. 14. Size of Ca(OH)<sub>2</sub> obtained from XRD as a function of BNP concentration

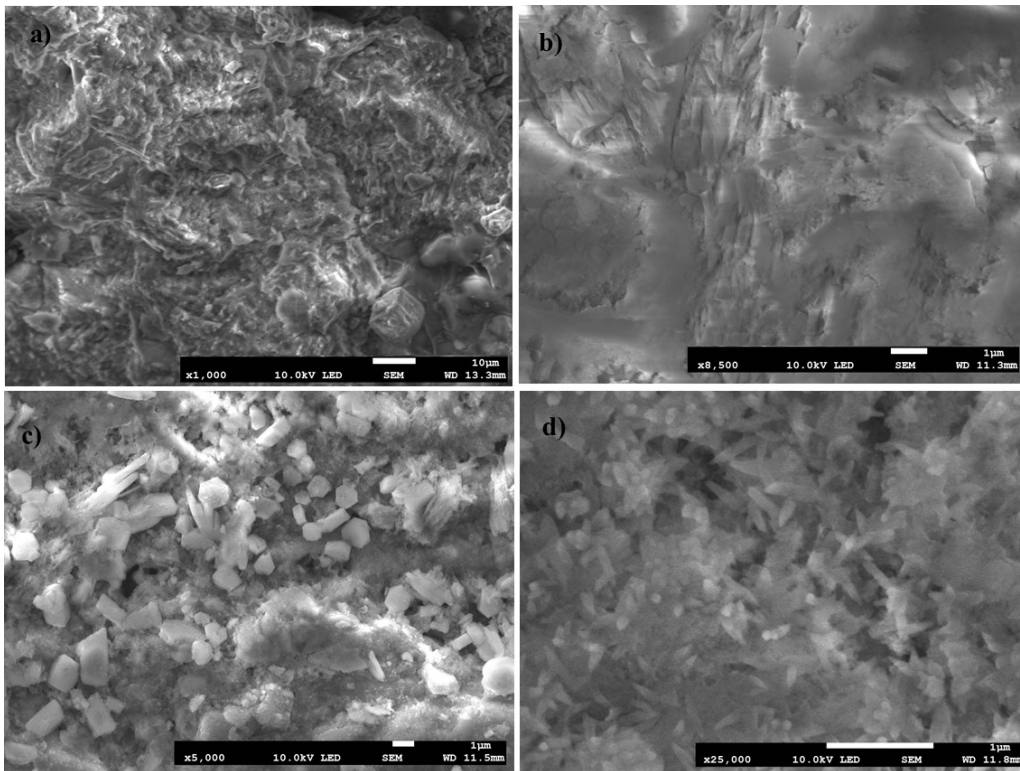


Fig.15. SEM micro images of the cementitious composites at 7 days. a) plain cementitious composite, b) with 0.20-wt% BNPs, c) with 0.40-wt% BNPs, d) with 0.60-wt% BNPs

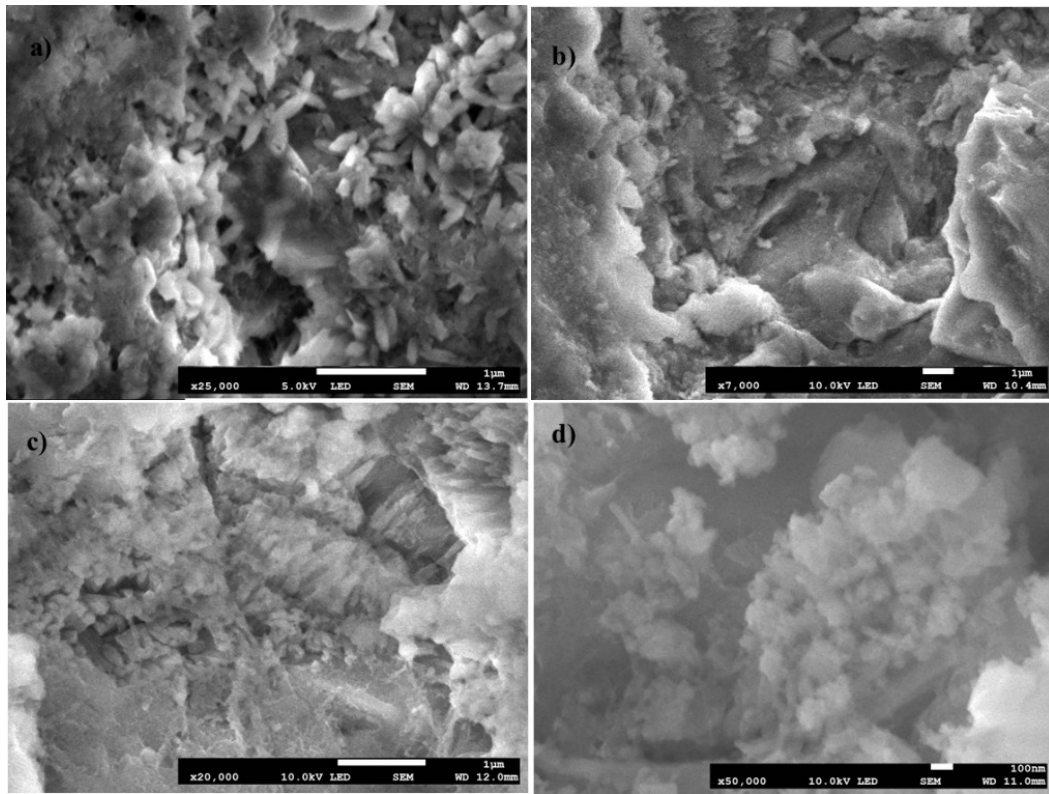


Fig.16. SEM micro images of the cementitious composites at 14 days. a) plain cementitious composite, b) with 0.20-wt% BNPs, c) with 0.40-wt% BNPs, d) with 0.60-wt% BNPs

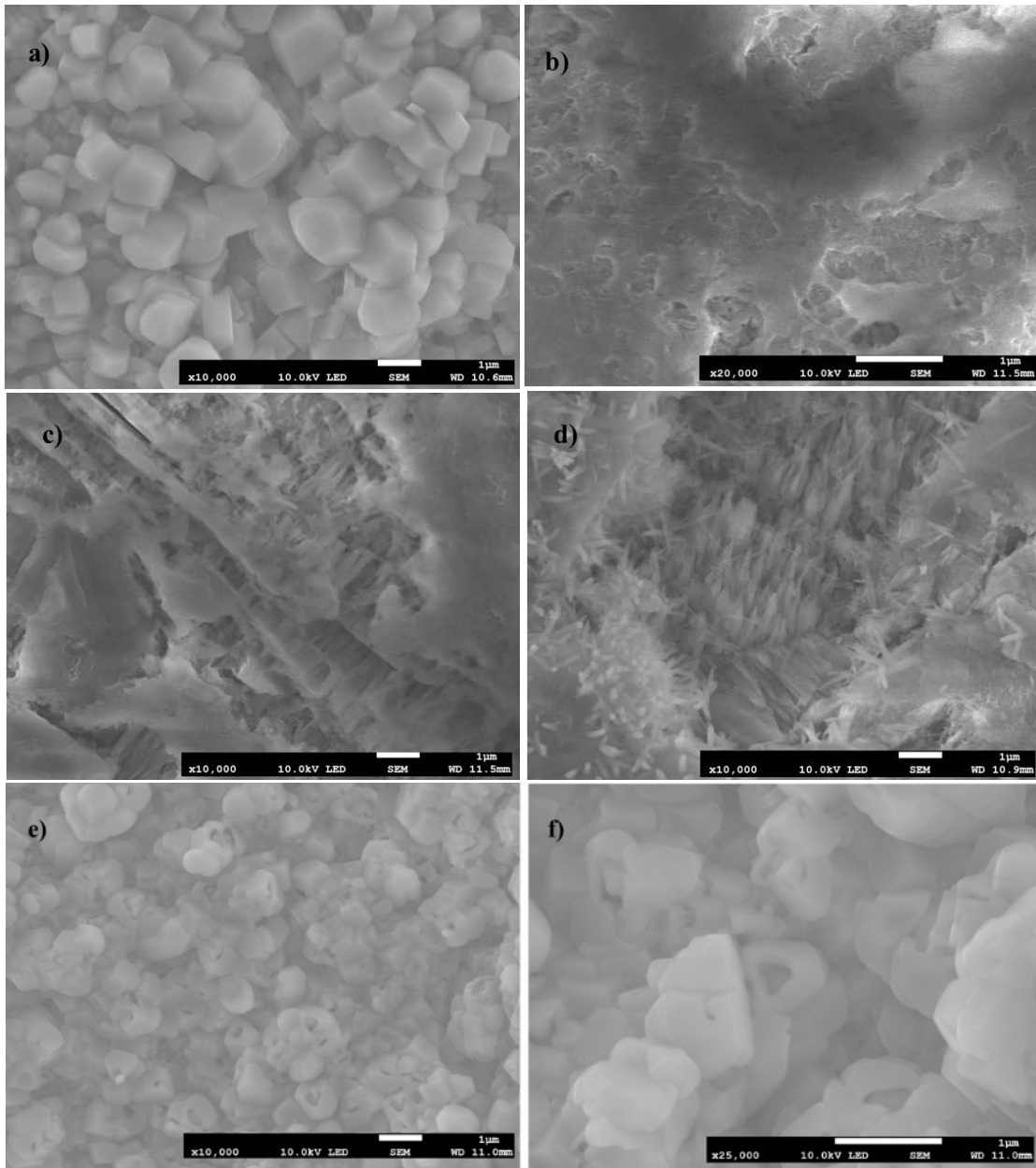


Fig.17. SEM micro images of the cementitious composites at 28 days. a) plain cementitious composite, b,c) with 0.20-wt% BNPs, d) with 0.40-wt% of BNPs, e,f) with 0.60-wt% of BNPs

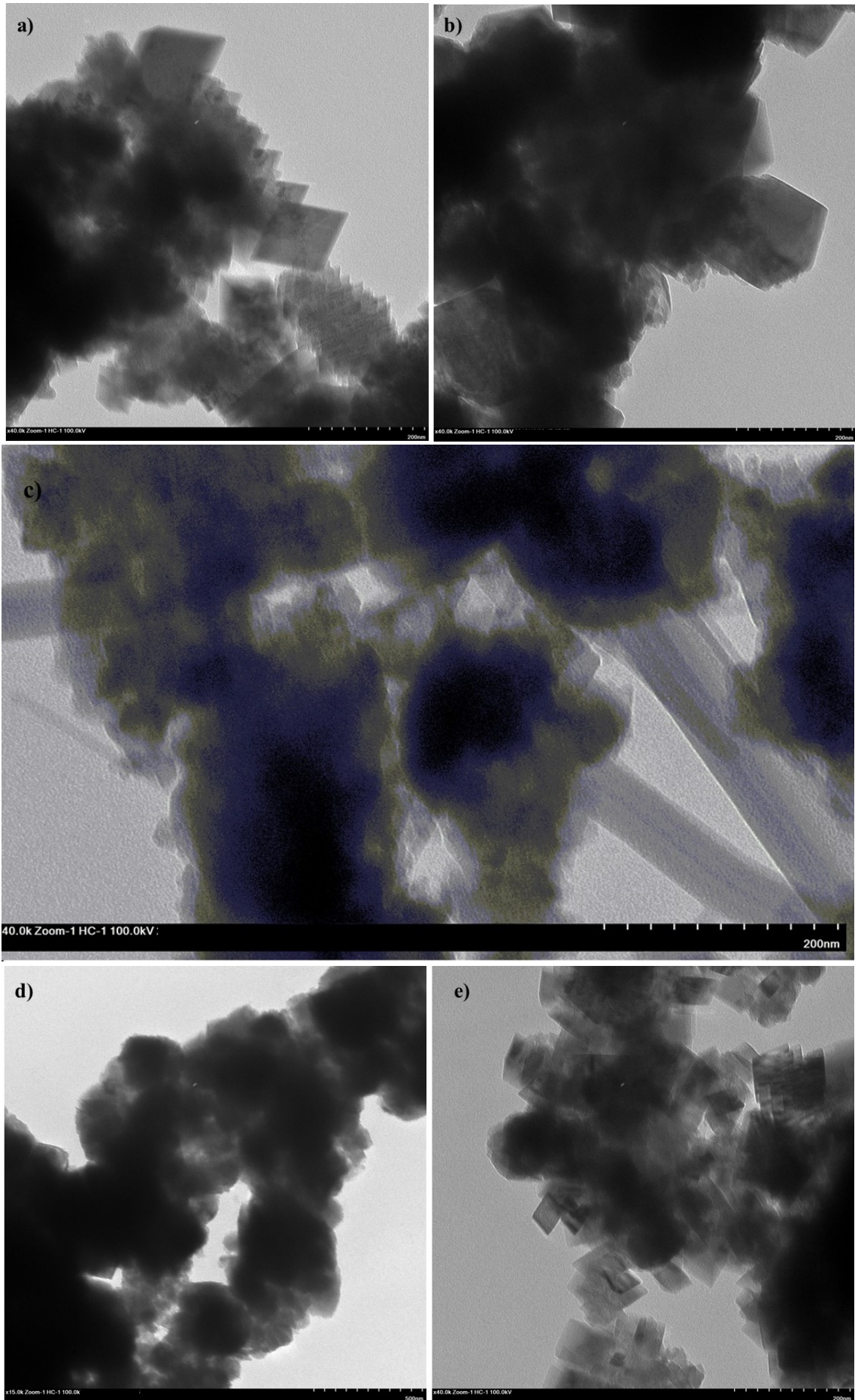


Fig. 18. TEM micro images at 28 days of curing a) plain cementitious composite, b,c) with 0. 20-wt% BNPs, c) with 0. 20-wt% BNPs showing fabrics-like crystals, d) with 0.40-wt% BNPs, e) with 0.60-wt% BNPs

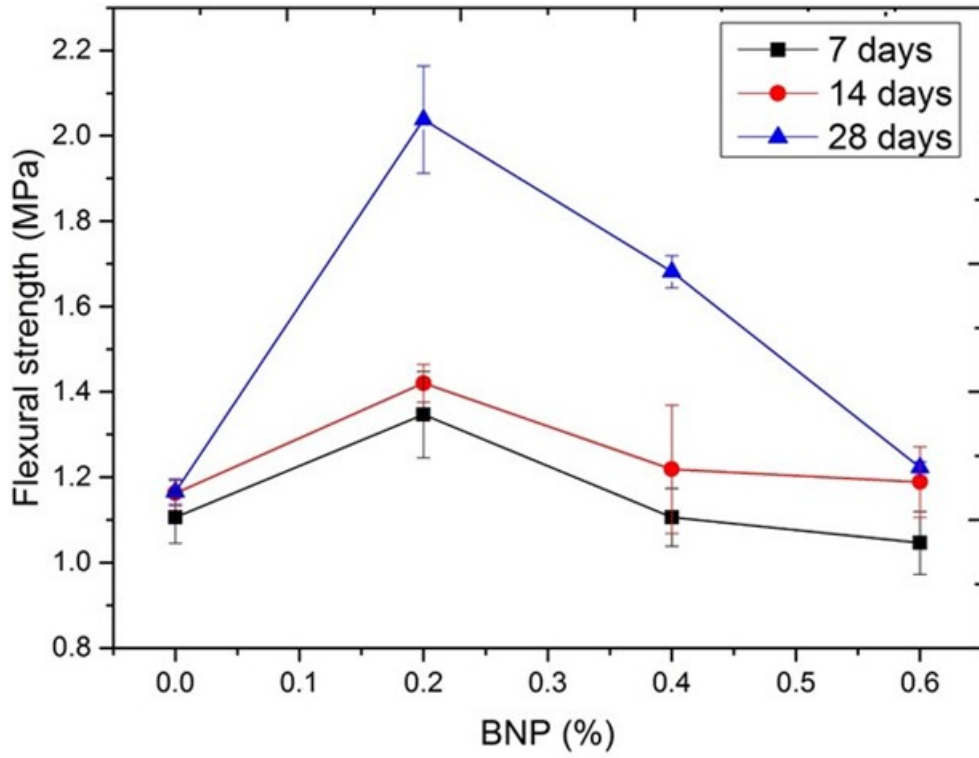


Fig. 19. Variation of the flexural strength as a function of BNP concentration at different curing ages

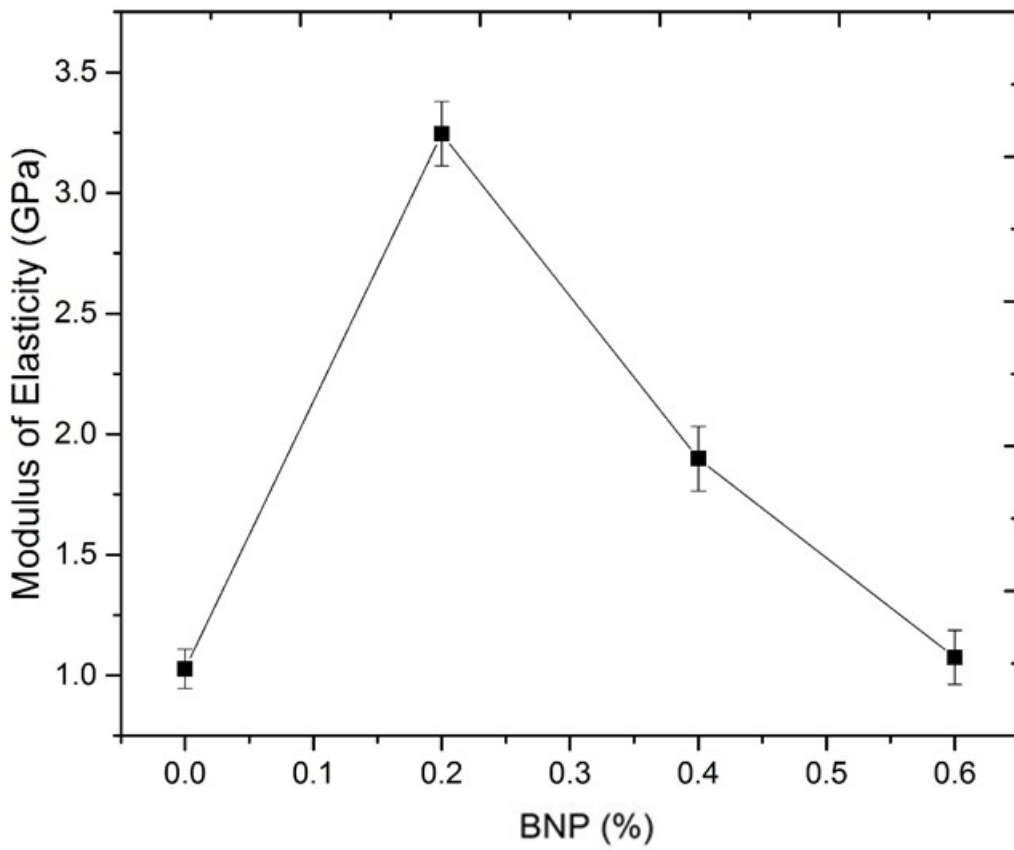


Fig. 20. Variation of the modulus of elasticity as a function of BNP concentration at 28 days

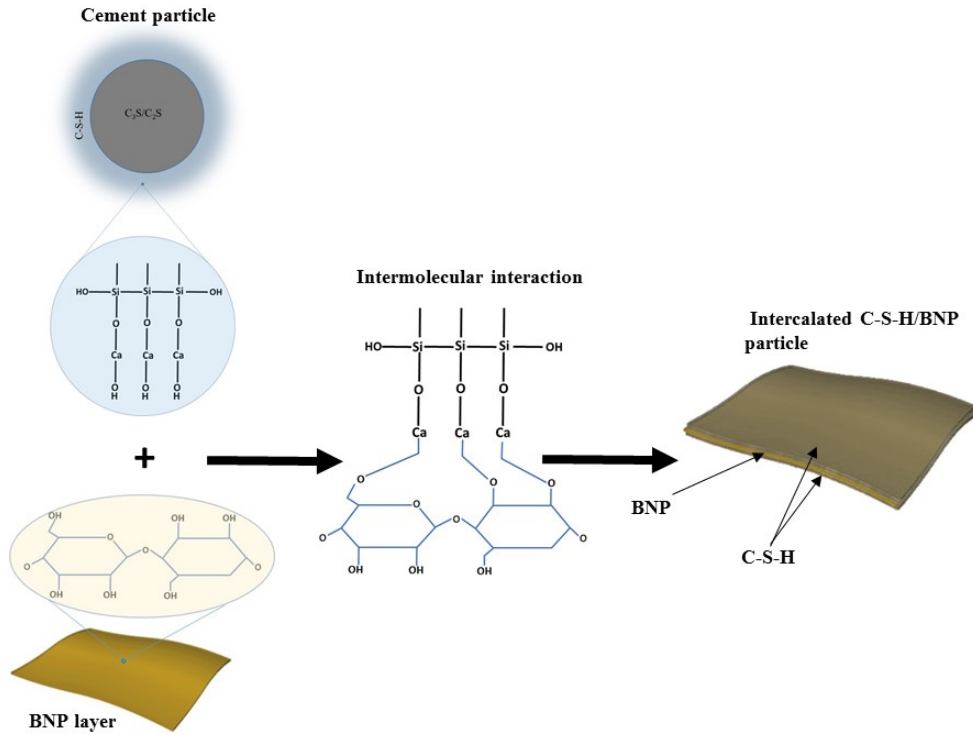


Fig. 21. Schematic illustration of intermolecular interaction of BPN with C-S-H phase at 28 days.

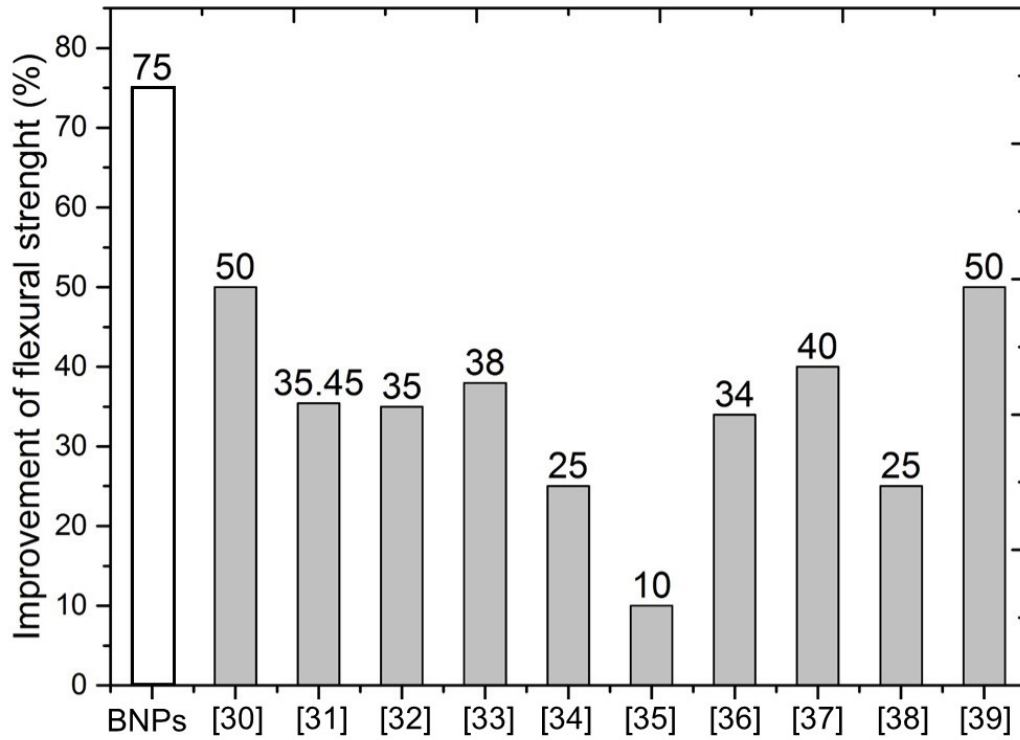


Fig. 22. Comparison of maximum flexural strength of BNP-cementitious composites and MWCNT-cementitious composites from References [30-39] in terms of percentage increase.

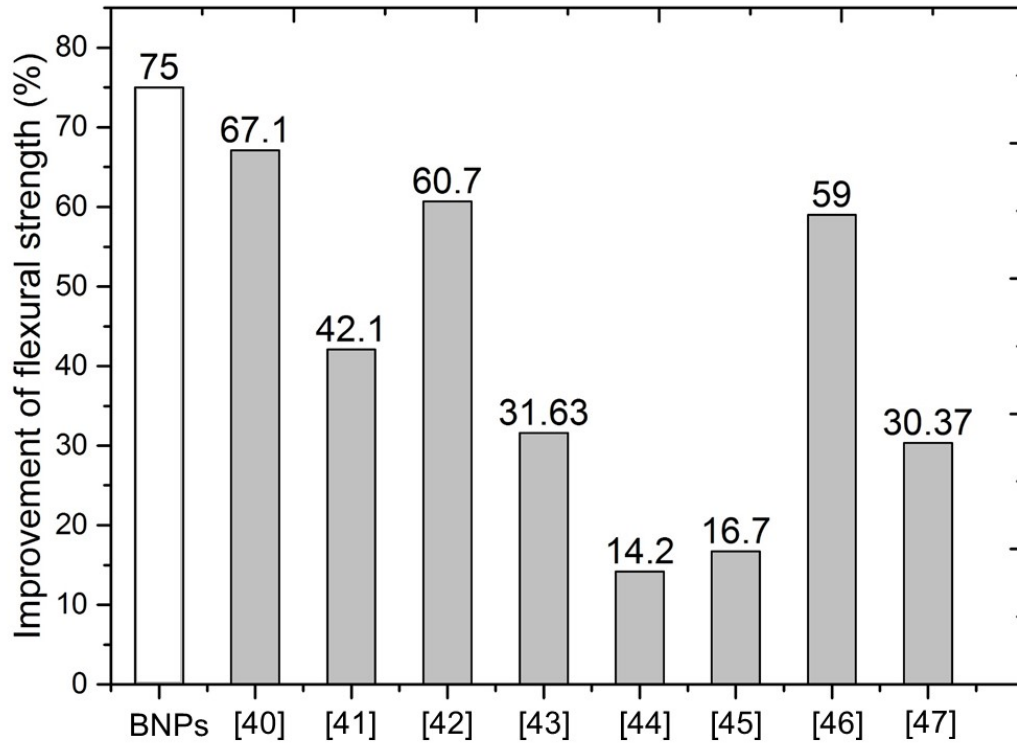


Fig. 23. Comparison of maximum flexural strength of BNP-cementitious composites and GO-cementitious composites from References [41-48] in terms of percentage increase.

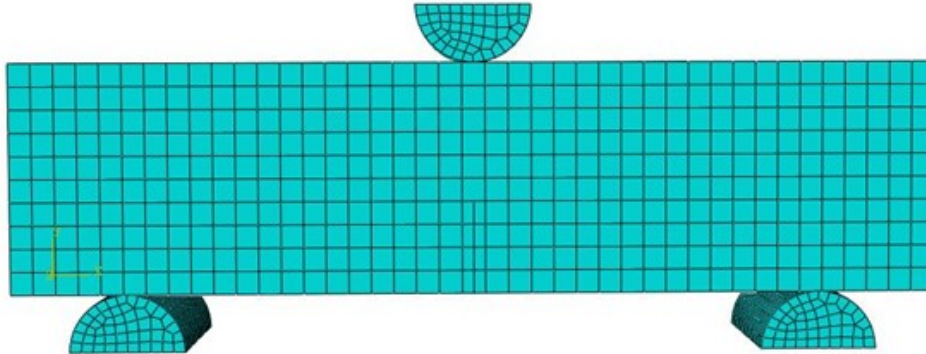


Fig. 24. X-FEM model of the notched cementitious composite prism for fracture modelling and analysis

Table 2. Average material properties of the cementitious composites

Material	Flexural strength (MPa)	Modulus of Elasticity (GPa)	Fracture Energy (N/M)
Plain cement	1.2	1.12	12.55
With 0.20-wt% BNPs	2.1	3.25	23.60

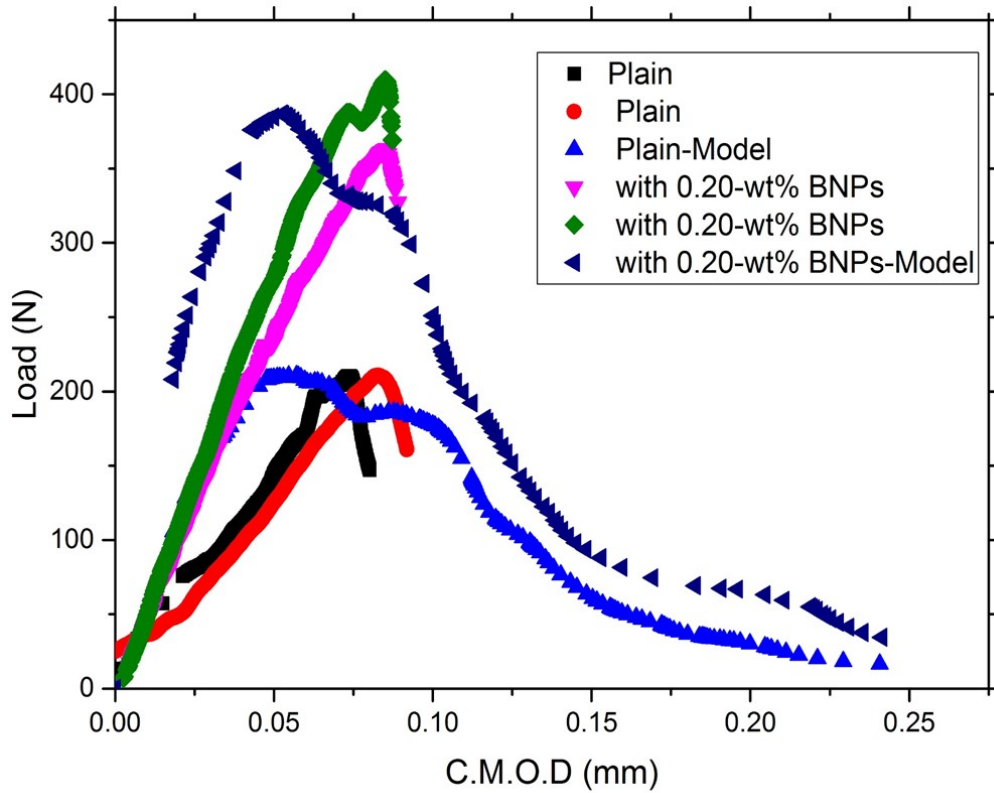


Fig. 25. Load versus crack mouth opening displacement for cementitious composites with and without 0.20-wt% BNPs. experimental versus modelling.

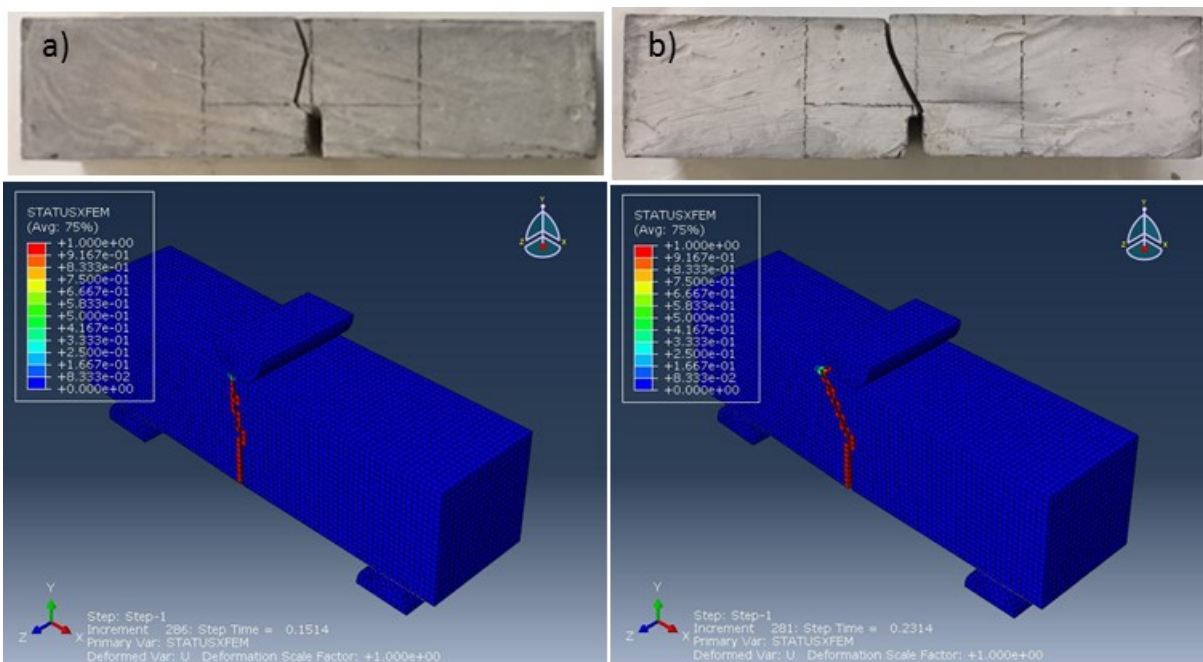


Figure 26. Experimental and simulated fracture behavior of the cementitious composite beams. a) plain cement prism, b) with 0.20-wt% BNPs.

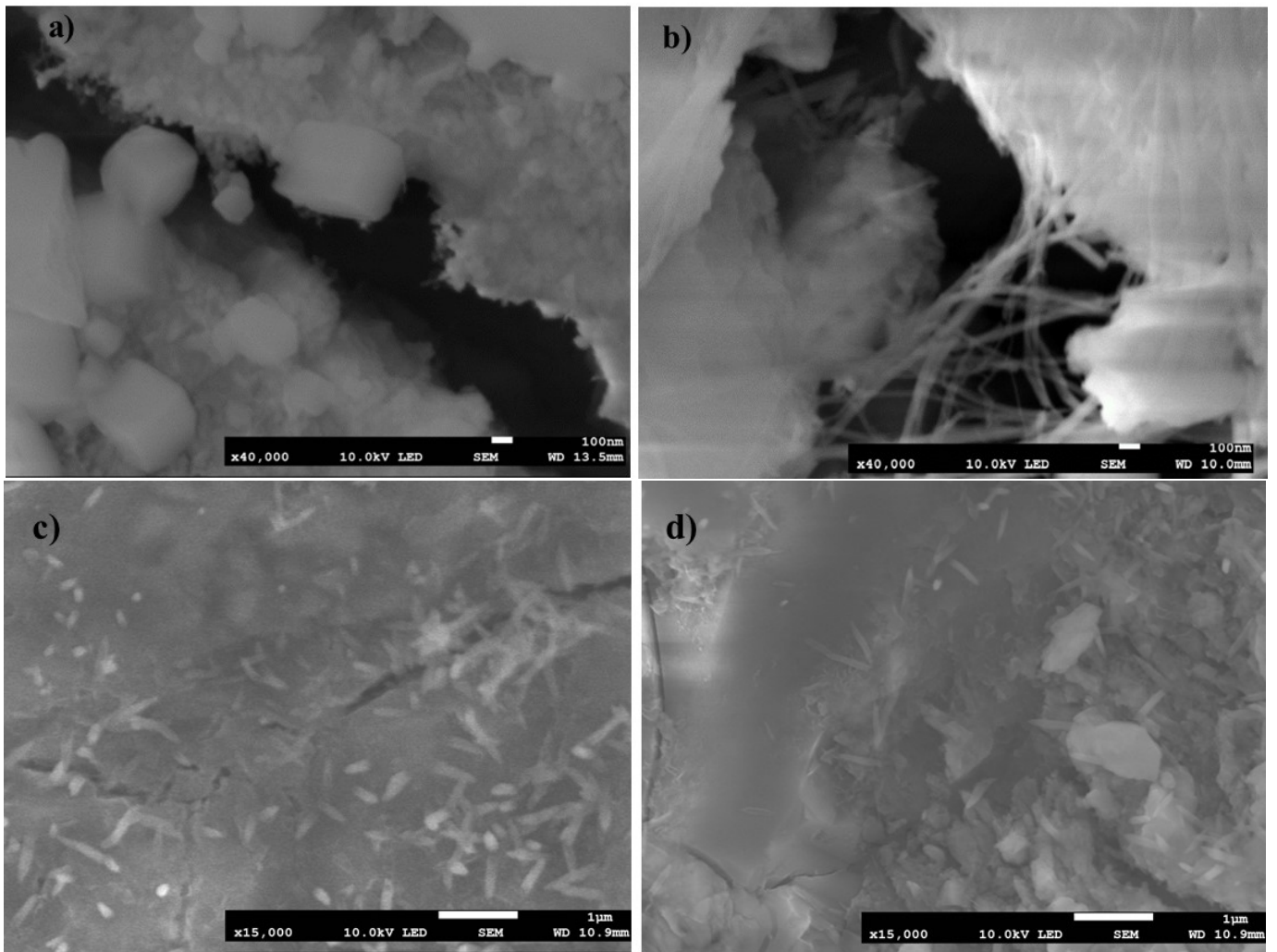


Fig. 27. SEM micro image showing crack propagation in a) plain cementitious composite, b) with BNPs showing BNP crack bridging, c and d) with BNP showing crack deflection